Journal Pre-proof

Lithological and structural control on fracture frequency distribution within a carbonate-hosted relay ramp

Marco Mercuri, Eugenio Carminati, Maria Chiara Tartarello, Marco Brandano, Paolo Mazzanti, Alessandro Brunetti, Ken J.W. McCaffrey, Cristiano Collettini

PII: S0191-8141(19)30538-3

DOI: https://doi.org/10.1016/j.jsg.2020.104085

Reference: SG 104085

To appear in: *Journal of Structural Geology*

Received Date: 20 December 2019

Revised Date: 4 May 2020

Accepted Date: 4 May 2020

Please cite this article as: Mercuri, M., Carminati, E., Tartarello, M.C., Brandano, M., Mazzanti, P., Brunetti, A., McCaffrey, K.J.W., Collettini, C., Lithological and structural control on fracture frequency distribution within a carbonate-hosted relay ramp, *Journal of Structural Geology* (2020), doi: https://doi.org/10.1016/j.jsg.2020.104085.

CRediT authorship contribution statement

M. Mercuri: Conceptualization, Methodology, Validation, Investigation, Visualization, Writing – Original Draft. **E. Carminati**: Conceptualization, Writing – Review and Editing, Supervision, Funding acquisition. **M. C. Tartarello**: Investigation, Writing – Review and Editing. **M. Brandano**: Investigation, Writing – Review and Editing. **P. Mazzanti**: Methodology, Data Curation, Writing – Review and Editing. **A. Brunetti**: Methodology, Data Curation. **K. J. W. McCaffrey**: Methodology, Writing – Review and Editing, Supervision. **C. Collettini**: Conceptualization, Writing – Review and Editing, Supervision

Lithological and structural control on fracture frequency distribution within a carbonate-hosted relay ramp

Marco Mercuri[a], Eugenio Carminati[a], Maria Chiara Tartarello[a], Marco Brandano[a], Paolo Mazzanti[a,b], Alessandro Brunetti[b], Ken J. W. McCaffrey[c], and Cristiano Collettini[a]

Affiliation addresses:

[a] Dipartimento di Scienze della Terra, Sapienza Università di Roma, Piazzale Aldo Moro 5, 00185, Rome, Italy

[b] NHAZCA S.r.l., spin-off company Sapienza Università di Roma, Via Vittorio Bachelet 12, 00185 Rome, Italy

[c] Earth Sciences Department, Durham University, South Road, Durham, DH1 3LE, UK

E-mail addresses: marco.mercuri@uniroma1.it (M. Mercuri), eugenio.carminati@uniroma1.it (E.Carminati), mariachiara.tartarello@uniroma1.it (M. C. Tartarello), marco.brandano@uniroma1.it (M. Brandano), paolo.mazzanti@uniroma1.it (P. Mazzanti), alessandro.brunetti@nhazca.com (A. Brunetti), k.j.w.mccaffrey@durham.ac.uk (K. J. W. McCaffrey), cristiano.collettini@uniroma1.it (C. Collettini).

*corresponding author: tel. +393342844933; e-mail: marco.mercuri@uniroma1.it; postal address: Dipartimento di Scienze della Terra, Sapienza Università di Roma, Piazzale Aldo Moro 5, 00185 Rome, Italy

keywords: fractures; virtual outcrop; FracPaQ; carbonate facies; relay ramp

Abstract

Understanding the factors controlling fracture frequency distribution can greatly improve the assessment of fluid circulation in fault damage zones, with evident implications for fault mechanics, hydrogeology and hydrocarbon exploration. This is particularly important for relay zones that are usually characterized by strong damage and structural complexity. We investigated the fracture frequency within an outcrop adjacent to the front fault segment of a relay ramp, hosted within peritidal carbonates that forms part of the Tre Monti fault (Central Italy). We analysed the distribution of fracture frequency in the outcrop through (1) scanlines measured in the field, (2) oriented rock samples, and (3) scan-areas performed on a virtual outcrop model. Fracture frequency increases with distance from the front segment of the relay ramp. Moreover, supratidal and intertidal carbonate facies exhibit higher fracture frequency than subtidal limestones. This trend of increased fracture frequency has two main explanations. (1) The number of subsidiary faults and their associated damage zones increases moving away from the front segment. (2) the supratidal and intertidal carbonate facies content increases toward the centre of the relay ramp. Our results indicate that the fracture frequency pattern is very complex in relay ramps hosted in shallow-water limestones and that its prediction necessitates a good control on structures and sedimentary facies distribution.

1. Introduction

Fractures in the damage zone (Chester and Logan, 1986; Chester et al., 1993) constitute the main pathway for fluids within faults hosted in low-porosity rocks (Caine et al., 1996; Aydin, 2000; Gudmundsson et al., 2001; Bense et al., 2013; Bigi et al., 2013). Fracture frequency and the variation of geometrical and topological properties of fracturing in space are an important control on permeability, and hence on fluid flow and fault mechanics. For example, these variations in these attributes may control traps and leakage points within hydrocarbon reservoirs affected by the presence of faults and promote or prevent local fluid overpressures. A poorly connected fracture

system might lead to the development of high fluid pressures, which can in turn influence the evolution of the stress state (Sibson, 1994) with profound implications for earthquake triggering (e.g., Nur and Booker, 1972; Miller et al., 2004). Conversely, a well-connected fracture system prevents the development of fluid overpressures and this leads to the maintenance of a strong but critically stressed crust (Townend and Zoback, 2000). Furthermore, fracture distribution can have a direct effect on fault mechanics: a change of elastic properties of host rock promoted by fracturing may lead to a stress field rotation within damage zone, allowing reactivation of unfavourably orientated faults (Faulkner et al., 2006). Characterization of fracture distribution and its controlling factors is therefore fundamental to better understand fluid circulation and mechanics of fault zones, with obvious consequences for hydrogeology and hydrocarbon exploration. Assessing fracture distribution is particularly relevant for relay ramps (and generally, for zones of faults interaction) as they are commonly characterized by stronger damage than isolated fault segments (Kim et al., 2004; Peacock et al., 2017) and by high structural complexity (Kattenhorn et al., 2000; Peacock et al., 2000; Peacock and Parfitt, 2002; Fossen et al., 2005; Ciftci & Bozkurt, 2007; Bastesen and Rotevatn, 2012; Peacock et al., 2017), with important consequences for fluid flow (Sibson, 1996; Rotevatn et al., 2007; Fossen and Rotevatn, 2016 and references therein).

Here we integrate classical and modern structural geology techniques to investigate the fracture frequency distribution and its controlling factors within a well-exposed portion of a carbonate-hosted relay ramp damage zone that is part of the Tre Monti fault, a normal fault in the Central Apennines of Italy. We observe that lithology (carbonate facies) and the distribution of secondary faults accompanying relay ramp development play an important role in the fracture density.

1.1. Factors controlling fracture distribution within fault zones.

Many field and laboratory studies have been carried out to investigate factors controlling fracture distribution within fault zones. A first factor is represented by distance from the main fault: both microfracture and fracture density generally increase moving toward fault core (Brock and

Engelder, 1977; Wilson et al., 2003; Faulkner et al., 2006; Mitchell and Faulkner, 2009). However, fracture intensity does not scale with displacement accommodated by the main fault (Anders and Wiltschko, 1994; Shipton and Cowie, 2003). This has been attributed to the existence of a critical value of deformation intensity marking the transition from a strain hardening to a strain softening behaviour induced by the development of slip surfaces (Shipton and Cowie, 2003). Instead, higher displacements accommodated by faults lead to an increase in the damage zone thickness until a critical width is reached (Shipton and Cowie, 2001, 2003; Mitchell and Faulkner, 2009; Savage and Brodsky, 2011). This can be attributed to a continuous development of subsidiary faults producing their own damage zone (Shipton and Cowie, 2003). Other fault-related factors that influence distribution and the geometrical/topological properties of fractures are related to the stress field. For example, the asymmetric pattern of the stress field occurring during the long-term propagation of a fault (Berg and Skar, 2005), and rupture directivity during earthquakes (Dor et al., 2006a, 2006b; Mitchell et al., 2011) may produce an asymmetric damage distribution between hangingwall and footwall, whilst development of local stresses may promote a deflection of fractures (Gudmundsson et al., 2010).

Lithology plays another important role in fracture frequency distribution. A stratigraphic or tectonic juxtaposition of different lithologies leads to contrasts in mechanical properties (e.g., brittleness; Peacock and Xing, 1994) causing a mechanical layering that influences deformation pattern (Tavani et al., 2008), and fracture spacing, propagation and arrest (Odling et al., 1999; McGinnis et al., 2017). In general, fractures tend to form in more brittle layers and they often arrest at interfaces where mechanical contrasts are present (e.g., bedding). For carbonate lithologies, even a variation in carbonate facies at metric to decametric scale can affect fracturing (Wennberg et al., 2006; De Paola et al., 2008; Larsen et al., 2010a, 2010b; Michie et al., 2014; Rustichelli et al., 2016; Volatili et al., 2019). For example, Rustichelli et al. (2016) observed higher fracture intensity, trace length and connectivity in platform compared to ramp carbonates, whilst Larsen and co-authors (2010a, b) found that fractures forming in the subtidal facies tend to arrest in proximity to intertidal laminated

limestones. Finally, thickness of sedimentary beds can influence fracturing: a widely observed relationship is that, for strata-bound fractures, fracture intensity is inversely proportional to bed thickness (Ladeira and Price, 1981; Pollard and Aydin, 1988; Huang and Angelier, 1989; Narr and Suppe, 1991; Wu and Pollard, 1995; Bai and Pollard, 2000).

1.2. The structure-from-motion algorithm to build virtual outcrops

In this study we integrate classical field techniques (i.e., scanlines; Wu and Pollard, 1995) and a virtual outcrop (Bellian et al., 2005; McCaffrey et al., 2005a, 2005b) to investigate fracture frequency distribution and its controlling factors in a relay ramp system formed in carbonate host rocks.

In the last decade, virtual outcrops have been extensively used in structural geology (Bemis et al., 2014; Telling et al., 2017 for a review), and in particular for studies dealing with fractures (Olariu et al., 2008; Vasuki et al., 2014; Pless et al., 2015; Casini et al., 2016; Seers and Hodgetts, 2016; Corradetti et al., 2017; Bonali et al., 2019 and many others). The employment of virtual outcrops in geology has increased our ability and efficiency to collect data, allowing the collection of high-precision georeferenced datasets, also from inaccessible portions of the outcrop (Bellian et al., 2005; McCaffrey et al., 2005a, 2005b). An increasingly adopted methodology to build virtual outcrops is represented by the structure-from-motion technique (Westoby et al., 2012; Bemis et al., 2014; Colomina and Molina, 2014; Tavani et al., 2014; Vasuki et al., 2014; Bistacchi et al., 2015; Bonali et al., 2019), because it has a higher efficiency to cost ratio than other techniques such as laser scanning (LiDAR) (Wilkinson et al., 2016; Cawood et al., 2017). The structure-from-motion algorithm exploits a series of overlapping photos taken from various positions by a person or a drone (UAV, Unmanned Aerial Vehicle) to build a 3D model of the scene (Bemis et al., 2014). The model can be sized and georeferenced using the knowledge of the geographic position of some objects (i.e., ground control points) in the scene (Bemis et al., 2014). For this study, the

employment of a virtual outcrop allowed us to accurately map the fracture distribution in our study outcrop.

2. Geological setting

2.1. The central Apennines tectonic framework

The central Apennines are an active NE to ENE verging fold-and-thrust belt that started to form in the late-Oligocene in response to the westward directed subduction of the Adria plate beneath the European plate (Doglioni, 1991; Carminati et al., 2010). Thrusting scraped-off and piled up the sedimentary sequence overlying the continental basement of Adria, including a shallow- to deep-water Upper Triassic to Middle Miocene carbonate succession (Cosentino et al., 2010 and references therein). Since the Early Pliocene, NE-SW oriented extension started to act in the Central Apennines to the west of the compressive front, in response to the opening of the Tyhrrenian back-arc basin (Doglioni, 1991). The compressive-extensional couple has continuously migrated to the northeast (Cavinato and De Celles, 1999). Extension is currently active in the Central Apennines (D'Agostino et al., 2001a; Devoti et al., 2010) and is accommodated by normal faults striking mainly NW-SE, although rare SW-NE trending fault, such as the Tre Monti fault are present (Fig. 1a). These faults cut through both the pre-orogenic carbonates and the syn-orogenic flysch deposits (Fig. 1a), and their activity is manifest in the numerous earthquakes that have affected Italy in the recent past, such as the L'Aquila 2009 (Chiaraluce, 2012 and references therein), and the 2016-17 central Italy seismic sequences (Chiaraluce et al., 2017; Scognamiglio et al., 2018). The exhumation associated with the uplift that accompanies the extensional tectonic regime (D'Agostino et al., 2001b; Devoti et al., 2010) has exposed formerly buried active normal faults that now usually constitute the borders of the intermountain basins. The Tre Monti fault forms the north-west borders of the Fucino intermontane basin (Fig. 1a). In the Fucino basin, thrusting occurred from the Late Miocene to Early Pliocene, whilst the extensional tectonics started in the Late Pliocene and is still ongoing, as testified by the 1915 Avezzano earthquake (e.g., Galadini and Galli, 1999).

154

155 *2.2. The Tre Monti fault*

156 Tre Monti fault has been exhumed from a depth < 3 km (Smeraglia et al., 2016) and crops out as a
157 series of right-stepping, SE dipping fault scarps for a length of ~ 7 km (Fig. 1b). The fault
158 accommodates a throw that varies from ~ 0.7 km in the SW to ~ 2 km towards the NE (Smeraglia et
159 al., 2016). The fault scarps juxtapose Early Cretaceous to Miocene carbonates in the footwall with
160 Pliocene to Holocene continental deposits in the hangingwall (Fig. 1a, b). The predominance of dip
161 slip slickenlines on the main fault scarps (Fig. 1b; See also Morewood and Roberts, 2000;
162 Smeraglia et al., 2016; Mercuri et al., 2020) and paleoseismological investigations (Benedetti et al.,
163 2013; Cowie et al., 2017) indicate that the Tre Monti fault has been active as a normal fault since
164 the Pliocene, probably acting as a release fault (sensu Destro, 1995) for the San Potito – Celano
165 fault (SPCF; Fig. 1a). Finally, the Tre Monti fault has experienced past earthquakes, as suggested
166 by microstructural studies of the fault core (Smith et al., 2011; Smeraglia et al., 2016, 2017).
167 A key outcrop for the Tre Monti fault zone structure is provided by an abandoned quarry located ~
168 2 km WSW of Celano village (42°04’35’’N 13°30’00’’E; see also Fig. 1a, b). The quarry is located
169 within a portion of a relay zone delimitated by two right-stepping segments on the main fault (zoom
170 in Fig. 1b) and has been named “La Forchetta quarry” in previous studies (Smeraglia et al., 2016,
171 2017, Mercuri et al., 2020). The quarry extends for ~ 200 m in a NE-SW direction and for ~ 100 m
172 in the NW-SE direction (inset of Fig. 1b). The south-eastern limit of the quarry is marked by the
173 front segment of the relay ramp (Fig. 1b-c), which dips (~55°) to the southeast (156° mean dip
174 azimuth) (Smeraglia et al., 2016, Mercuri et al. 2020; see also the stereoplot in Fig. 1c). The
175 slickenlines on the front segment indicate a right-transtensional to right-lateral kinematics (mean
176 rake 155°; see stereoplot in Fig. 1c). The kinematics observed here may be due to a stress field
177 rotation promoted by the interaction of the segments that border the relay zone (Mercuri et al.,
178 2020).

The fault damage zone is exposed in almost 360° perspective on the quarry walls (Fig. 1c) and is hosted by Lower Cretaceous limestones pertaining to the "*Calcari Ciclotemici a Gasteropodi e ooliti*" Formation (Centamore et al., 2006). They were deposited at the transition between tidal flat and lagoon carbonate platform environments (Fig. 2a) and are organized in metric-scale peritidal cycles (Fig. 2b), reflecting the variation of accommodation space (c.f., Osleger 1991; D'Argenio et al., 1997). The supratidal facies comprises light-gray to havana-brown poorly sorted grainstones with radial ooids and pisoids (Fig. 2e, h). The intertidal facies is defined by laminated, white coloured microbial bindstones with birdseyes and fenestrae (Fig. 2f, i). Finally, the subtidal facies is mainly composed of white packstones with peloids and oncoids (Fig. 2g, j), although some sporadic floatstones with gastropods and some oncoidal rudstones are present.

The bedding organization is strongly controlled by the relative abundance of the carbonate facies mentioned above. Where the supratidal and the intertidal are the most abundant facies, the limestones are arranged in cm- to dm- scale tabular beds (Fig. 2c). Conversely, a predominance of the subtidal facies has beds that are more than 1 m thick (Fig. 2d).

3. Methods

In this section, we present the methodology employed to extract fracture properties from scanlines (section 3.1), samples (section 3.2), and the virtual outcrop (section 3.3).

3.1. Scan-lines

We performed 26 scan-line surveys (Priest and Hudson, 1981; see the example in Fig. 3) in the quarry area (see Section S1.1 for their location). Length, position, and orientation of the scan-lines were chosen in order to maximise their length and to maintain a sub-horizontal direction in irregular outcrops. The effective length and the orientation of each scanline is reported in Table S4.1. The effective length of the scan-line surveys was calculated by subtracting portions of outcrop hidden by vegetation from their total length. For each scanline survey we collected trace lengths and

orientations of all the fractures (mostly joints, minor shear fractures, and rare veins) intersecting the measuring tape. For trace length analysis we considered only fractures having both the terminations visible (~94% of all collected fractures). Fracture orientation was investigated by producing contour plots with the software Stereonet (Allmendinger et al., 2012; Cardozo & Allmendinger, 2013). The contours account for the inhomogeneous sampling of fractures along a scanline depending on their orientation (Terzaghi, 1965). The Terzaghi correction (Terzaghi, 1965) was applied by inserting the trend and plunge of each scanline in the Stereonet software (Allmendinger et al., 2012; Cardozo & Allmendinger, 2013). When data from scanlines with similar orientations (coming from the same sector of the quarry) were plotted in a single stereoplot, we applied the Terzaghi correction by using the mean direction of the scanlines (e.g., Figure 6). We calculated the mean fracture spacing by dividing the effective length of the scanline for (N-1), where N is the number of fractures intercepted by the scan-line. The linear fracture frequency, or P10 (Sanderson and Nixon, 2015), was calculated as the reciprocal of the mean spacing (Fig. 3). Finally, we assigned a carbonate facies to each scanline through a visual inspection in the field (Table S4.1). Due to the nature of the quarry this was limited to the intertidal facies and supratidal facies only.

3.2. Samples

27 oriented hand-samples (Fig. 4a) were collected, mostly in the same locations as the scanlines (section S1.2). Oriented samples were cut along vertical sections striking ~ 155° N (i.e., parallel to the front fault segment dip), polished, and scanned at a 1200 dpi resolution. Fracture traces were digitized using a commercial vector graphic software (Fig. 4b). For each sample, we evaluated the fracture spacing, the linear and areal fracture frequency (P10 and P20 respectively; Sanderson and Nixon, 2015), and fracture intensity (P21; Sanderson and Nixon, 2015). The spacing and the linear fracture frequency (P10), were calculated by tracing a series of sub-parallel scanlines on each sample (Fig. 4c), and following the same procedure adopted for the “regular” scan-lines (section 3.1). The others fracture properties were extracted using the FracPaQ (v. 2.4) Matlab tool (Fig. 4d;

Healy et al., 2017). This software takes a .svg file containing the polylines of fracture traces as input, and, according to the parameters inserted by the user, calculates the fracturing properties mentioned above. We refer the reader to the paper of (Healy et al., 2017) for a complete description of the algorithms used by the FracPaQ software. For each sample, we inserted the appropriate pixel/m ratio, in order to obtain the outputs in unit length (Healy et al., 2017). Furthermore, a carbonate facies was assigned to each sample by visual inspection. The lists of fracture parameters obtained are summarised in section S4.2.

3.3. Fracture analysis on the virtual outcrop

The photos used for the structure-from-motion algorithm were captured by an Unmanned Aerial Vehicle survey performed with an Aeromax X4 quadcopter equipped with a Sony Alpha 5000 camera (Fig. 5a). We collected 650 photos with an overlap of ~ 70% between adjacent pictures. The workflow we adopted to build the 3D model is very similar to that described by other authors (e.g., Tavani et al., 2014; Bistacchi et al., 2015; Bonali et al., 2019): photos were aligned through a semi-automatic identification of common points in adjacent pictures in order to create a point cloud. The point cloud is subsequently used to build a mesh and, finally, a textured mesh, that is the virtual outcrop (Fig. 5b). The virtual outcrop was scaled and georeferenced with respect to a previous terrestrial laser-scanner survey (Mercuri et al. 2020). We constructed 6 ortho-mosaics (such as the one represented in Fig. 5c), with a resolution of 1 pixel per 1 cm, from the virtual outcrop, one for each quarry wall (labelled with capital letters in the inset in Fig. 6a). We subdivided each ortho-mosaic into several squares with 5 m side length, to form virtual scan-areas (Fig. 5c, d). The dimension of virtual scan-areas was established in order to have the side length bigger than most of the fracture trace lengths observed in scanlines (Fig. S2.1a). The location of all the virtual scan-areas is shown in Section S1.3. All the processing for the virtual outcrop and ortho-mosaic were executed within the 3DFlow Zephyr Aerial software. Each scan-area was manually interpreted in Adobe Illustrator® by drawing polylines, representing the traces of fractures, minor faults, and

bedding (Fig. 5e), and polygons to map the supratidal and the intertidal facies (Fig. 5f). The supratidal and intertidal facies were recognized by the visible cm to dm thick beds. The fracture analysis was performed in FracPaQ, using the same parameters as described in the previous section, to evaluate the areal fracture frequency (P20), fracture intensity (P21), and trace length. We also evaluated the minimum content of supratidal and intertidal facies in each scan-area by calculating their area in $pixel^2$ and dividing it by 250,000 px^2 (the scan-area). The fracture analysis results for each scan-area are reported in Section S4.3.

Finally, we captured 420 aerial photos using a Phantom 4 Pro quadcopter. The photos were processed using the same procedure described above to produce an aerial orthophoto of the quarry. This orthophoto was used as base map to check the position of all the georeferenced data we collected.

4. Results

Fractures in the quarry are mainly joints and shear fractures. Calcite-filled veins are quite rare and, if present, can be appreciated only at the hand sample scale. Fractures are accompanied by at least 80 minor faults with various orientations and kinematics (Fig. 6; see Mercuri et al., 2020 for further details). In the present study we distinguish the minor faults from the shear fractures by the presence of a fault core. Fractures exhibit a centimetre- to a meter-scale trace-length, with modal values between 10 and 50 cm (Section S2.1). The mean trace length calculated for each scanline is quite homogeneous throughout the whole quarry and generally smaller than 0.25 m (section S2.2). Virtual scan-areas suggest that the mean trace length is heterogeneous, with longer fractures located in the northern (trace lengths > 0.58 m) and in the western (0.46 m < trace length < 0.58 m) sectors of the quarry (S2.3). Most of the fractures are sub-vertical and E-W striking, while two minor clusters indicate the occurrence of sub-vertical fractures striking approximately NE-SW and NNW-SSE (Fig. 6). We do not observe any systematic cross-cutting relationship between the different fracture sets.

Although the entire quarry is characterized by high fracture frequency values, both scanlines and virtual scan-area show similar fracture frequency distribution patterns (Fig. 6). The portions of the quarry located immediately at the footwall of the front segment of the relay ramp are characterized by relatively low fracture frequency values (Fig. 6). On the SW side of the quarry (sectors E and F; see Fig. 6) the linear fracture frequency (P10) is lower than 25 m^{-1}, reaching a value of 10 m^{-1} close to front segment (for the scanline SL13; see S1.2 and S4.1), whilst the areal fracture frequency values (P20) are lower than 27 m^{-2}. The whole NE side of the quarry is characterized by relatively low fracture frequency values (Sector A in Fig. 6); in this sector the linear fracture frequency is generally lower than 28 m^{-1}, although it locally reaches values higher than 38 m^{-1} near the front segment (for the scanline SL12; see S1.2 and S4.1). High linear fracture frequency values (P10 ≥ 39 m^{-1}) are also located far from the front segment (for scanlines SL21 and 22; see S1.2 and S4.1). The areal fracture frequency is always smaller than 34 m^{-2} in the NE sector of the quarry. The portions of the quarry located far from the front segment of the relay ramp (sectors B, C, D; see Fig. 6) are characterized by the highest fracture frequencies. In detail the sectors B and D show areal fracture frequencies reaching values larger than 48 m^{-2}, up to 60 m^{-2} (Fig. 6, S4.3). Furthermore, the northern sector shows the highest concentration of minor faults, that are often associated with foliated breccias (Fig. 6). Breccias are characterized by anastomosing foliations, consisting of closely spaced undulated, striated slip surfaces, which are roughly parallel to the associated subsidiary faults (Fig. 7; see also Smeraglia et al., 2016). At hand-sample scale, the clasts are characterized by chaotic to crackle breccia textures (Woodcock and Mort, 2008; Smeraglia et al., 2016). The scan-area derived fracture intensity (P21) distribution mimics the distribution mentioned above (section S3.2).

In Figure 8 we show the variation in fracture frequency with distance from the principal fault in the quarry (i.e., the front segment of the relay ramp). Despite the high variability in fracture frequency for each fixed distance from the front segment, we recognize a general trend of fracture frequency increase moving away from the front segment (Fig. 8). The linear fracture frequency measured from

scanlines increases from a median value of 23 m^{-1} at distances < 60 m from the front segment to 32 m^{-1} at distances > 60 m (Fig. 8). Analogously, the areal fracture frequency measured from virtual scan-areas increases with distance from the front fault segment from a median value of 18 m^{-2} (distances < 60 m) to 29 m^{-2} (distances > 60 m) (Fig. 8). Conversely, we do not observe any particular relationship between fracture frequency/intensity distribution and distance from the front segment from data retrieved from the oriented samples (section S3.1.4).

We observe that supratidal and intertidal carbonates are more fractured than subtidal carbonates both in scanlines and oriented samples (Fig. 9a,b). The median of the linear fracture frequency retrieved from scanlines measured in supratidal and intertidal facies (28 m^{-1}) is ~40% larger than that measured in subtidal facies (20 m^{-1}) (Fig. 9a). Intertidal and supratidal oriented samples show median areal fracture frequencies (P20) that are respectively 170% (5.4×10^4 m^{-2}) and 100% (4.0×10^4 m^{-2}) higher than the subtidal samples (2.0×10^4 m^{-2}) (Fig. 9b). The relationship between fracture frequency and carbonate facies is clearer in virtual scan-areas (Fig. 9c), where the areal fracture frequency increases with the supratidal and intertidal content (Fig. 9c). In detail, fracture frequency ranges between 10 m^{-2} and 30 m^{-2} for supratidal and intertidal content <50%, whilst it reaches ~ 60 m^{-2} where the percentage is ~ 80 %.

5. Discussion

5.1 Classical field techniques vs. virtual outcrop models

Our data show a consistent fracture distribution in the fault damage zone in both data retrieved from the scanlines and from the virtual scan areas (Figs. 6, 8). The strong similarity of results produced by classical field techniques such as scanlines (Priest and Hudson, 1981; Wu and Pollard, 1995) and by the virtual scan areas, further demonstrates the high potential of virtual outcrops in structural geology (e.g., McCaffrey et al., 2005a, 2005b; Tavani et al., 2014; Bistacchi et al., 2015; Cawood et al., 2017). However, we do observe a small difference between the fracture trace length distribution

computed from scanlines and virtual scan areas (S2.1). This small discrepancy can be only partially attributed to the employment of a virtual outcrop. We believe that such a difference is due to two main biases. Firstly, scanlines are subjected to higher censoring effects (e.g., Priest and Hudson, 1981 among others) than virtual scan-areas. In fact, due to the vertical cliffs of the quarry, the sampling of vertical fractures longer than ~ 2 m - 3 m was impossible during most of the scanlines, whilst all the 5 m × 5 m virtual scan-areas allowed the collection of trace lengths smaller than 5 m. Secondly, scanlines allowed the collection of very small (< 10 cm) fractures that were quite impossible to identify in virtual scan-areas. The biases mentioned above produce a censoring of long fractures and oversampling of small fractures during scanlines, and this is evident when the histograms of trace lengths measured through the two methods are compared (S2.1).

The main advantage of using a virtual outcrop is the ability to collect fracture data on inaccessible or dangerous portions of the quarry. In this way we exploited most of the quarry wall surfaces for data collection (section S1.3), whilst only the base of the cliffs was analysed with scanlines for safety reasons (section S1.1). Since we manually interpreted the fractures, the employment of a virtual outcrop has not provided a consistent advantage in a matter of time efficiency. In fact, in addition to the generation of virtual outcrop model (photo acquisition and processing), which took about a week of work, the interpretation of each scan-area took approximately 2 hours, whilst the time needed for the data collection along a scanline in the field was ~2-3 hours. Despite the time requirements, the manual interpretation of fractures enabled us to preserve the interpretation ability of the user. In addition, the virtual scan-areas method enabled us to use the FracPaQ software (Healy et al., 2017) on the virtual outcrop models (Vinci et al., 2018; Giuffrida et al., 2019), which means that once the interpretation is complete it is easy to extract in a very short time (few minutes) a large number of fracture parameters. We believe that an important improvement in time-efficiency for the fracture analysis from virtual outcrops would be provided by the development of algorithms and workflows for the semi-automatic identification of fractures (e.g. Vasuki et al., 2014).

360

361 *5.2 Fracture density distribution*

362 The employment of scanlines allowed us to collect more than 1800 fracture attitudes (stereoplot in
363 Fig. 6) that were used as a control on the fracture frequency distribution obtained from the virtual
364 scan-areas. Fractures are mostly subvertical and strike in an E-W direction ($\pm$ 20°). The pole to
365 such an orientation is coherent with the orientation of the T axis obtained by inverting the kinematic
366 indicators on the front segment of the relay ramp (stereoplot in Fig. 1c). The other fracture sets
367 striking NE-SW and NNW-SSE (Fig. 6) are likely to be related to the evolution of the fault
368 structure. In particular, the NE-SW striking set is coherent with the orientation of the T axis
369 obtained by inverting the kinematic indicators collected on the entire Tre Monti fault (stereoplot in
370 Fig. 1b). The NNW-SSE striking fracture set can be interpreted as related to the development of the
371 relay ramp: bending of strata around an axis orthogonal to the main fault segments may lead to
372 ENE-WSW extension, consistent with the NNW-SSE striking joint set. The data on the widespread
373 population of fractures, i.e. those E-W striking, may be influenced by the direction of the scanlines,
374 most of them performed on NW-SE oriented quarry walls (Fig. 6; see also Fig. S1 and Table S4).
375 However, E-W striking fractures constitute the main set independently on the quarry wall
376 orientation (Figure 6), and therefore, if present, the bias induced by scanlines orientation is limited.
377 Although many studies have demonstrated that the fracture frequency in fault damage zones
378 increases moving toward the main fault segment (Brock and Engelder, 1977; Wilson et al., 2003;
379 Faulkner et al., 2006; Mitchell and Faulkner, 2009; Savage & Brodsky, 2011), in our case study
380 both scanlines and virtual scan-areas show that fracture frequency increases with distance away
381 from the most important fault in the outcrop, represented by the front segment of the relay ramp
382 (i.e., moving from SE to NW; Figs. 6, 8). The observed trend is not due to a geometric bias. Since
383 the most abundant set is E-W oriented, this has the biggest impact on the fracture density
384 calculation and we would expect the highest fracture density in the quarry sectors that have an
385 orientation close to N-S (e.g., sectors A, C, and E; see Fig. 6). Conversely, we observe the highest

fracture frequency in sectors B, C and D (Fig. 6). Therefore, if any geometric bias affects the absolute values of fracture frequency, it would lead to an underestimation of the rate of fracture frequency increase with distance from the front segment of the relay ramp.

We interpret this unusual trend of fracture frequency to be the result of two main factors. The first control is structural and related to the higher density of minor faults away from the front segment of the relay ramp (i.e., in the north-western sector of the quarry; Figs. 6, 10, 11a). In this scenario, due to the direct relationship between the number of fractures and faults, relatively higher fracture frequencies reflect the development of fractures pertaining to the damage zones of the subsidiary faults (e.g., Shipton and Cowie, 2003). The second important control on fracture distribution is played by lithology and, in particular, by the carbonate facies. Approaching the centre of the relay zone we document an increase in supratidal/intertidal facies (Fig. 11) that are characterized by a higher fracture frequency (Fig. 9).

The role of different carbonate facies in fracture density is further testified by fracture frequency measured on oriented samples showing that supratidal and intertidal rock samples are more fractured than the subtidal samples (Fig. 9b). Other authors have shown that carbonate facies can control fracture spacing in shallow-water limestones because of different Dunham's textures (Wennberg et al., 2006; Larsen et al., 2010b) or different mechanical properties (e.g., Giorgetti et al., 2016; Rustichelli et al., 2016). In particular, Wennberg et al. (2006) show that carbonate facies can be even more important than the mechanical layer thickness if the interbeds are strong (e.g., absence of a well-developed bedding). In our case study, the effect of carbonate facies on fracture frequency is related to the supratidal/intertidal facies being characterized by thinner bedding (cm- to dm- scale) facilitating a larger fracture frequency (Ladeira and Price, 1981; Pollard and Aydin, 1988; Huang and Angelier, 1989; Narr and Suppe, 1991; Wu and Pollard, 1995; Bai and Pollard, 2000).

Independently of the cause, the alternation of subtidal and intertidal/supratidal lithofacies at the outcrop scale is responsible for the formation of a mechanical stratigraphy, with strongly fractured

intervals confined in the supratidal/intertidal facies beds (Fig. 12a,b; see also Fig. 5e-f). The relative content of supratidal/intertidal facies plays an important role also in the deformation style developed in the northern sector of the study outcrop, which is characterized by the presence of foliated breccias (Fig. 11a). We suggest that during the fault activity, the high fracturing within the supratidal/intertidal facies increased permeability, favouring the influx of fluids into these portions of the relay zone. Fluids reacted with the fine grains within the fractured rocks promoting fluid-assisted dissolution and precipitation mass transfer processes (i.e., pressure-solution; Rutter, 1983; Gratier et al., 1999; Collettini et al., 2019). In addition, small amounts of clay minerals present in the supratidal facies (Strasser et al 1999; Fig. 12c) may further enhance pressure-solution (Gratier et al., 1999; Renard et al., 2001).

Since the quarry intercepts only a portion of the relay ramp (see Fig. 10), no constraints allow us to evaluate whether the fracture intensity distribution was prevalently structurally or lithologically controlled. We provide two end-member scenario depending on the main controlling factor on fracture distribution. In a first more conservative scenario, it is assumed that the distribution of carbonate facies is homogeneous and facies variations control fracture frequency only at metric to decametric scale (Fig. 13a). As a consequence, the increase of fracture frequency away from the front segment of the relay ramp is related to tectonic factors, such as the presence of an incipient breaching zone between the front and rear segment of the relay ramp that is not directly observable in map view because it is hidden by the presence of Pleistocene breccias (Fig. 13a; see also Fig. 1b). A clue for the presence of a breaching zone may be represented by the numerous subsidiary faults in the northern sector of the quarry. In this case, the increase in fracture frequency with distance from the front segment would be explained by the abandoned quarry intercepting the damage caused by the incipient breaching zone (Fig. 13a). In a second scenario, the distribution of carbonate facies is assumed as heterogeneous (Fig. 13b). As a consequence, the damage is heterogeneously distributed, and relatively higher fracture frequency is expected to follow the primary distribution of supratidal carbonate facies (Fig. 13b). According to this hypothesis, the

increase of fracture frequency moving away from the fault segment of the relay ramp would be explained by the presence in the northern sector of the study outcrop, of a stratigraphic interval characterized by a high supratidal facies content (Fig. 13b).

Our results indicate that fracture frequency pattern is very complex in relay ramps hosted in shallow-water limestones and that its prediction necessitates a good control on structures and sedimentary facies distribution. We suggest that both of these factors should be considered during fluid flow modelling within relay ramps hosted in shallow water limestones.

6. Conclusions

We evaluated the fracture distribution and its controlling factors within a relay ramp damage zone hosted in shallow water limestones. Combining classical (i.e., scanlines) and modern (i.e., virtual scan-areas) techniques, we have shown that fracture frequency increases moving toward the centre of the relay zone. Two main factors can explain this trend:

1) The number of subsidiary faults and their associated damage zones accommodating the development of the relay ramp increases moving toward the centre of the relay zone.

2) The supratidal and intertidal carbonate facies abundance increases toward the centre of the relay zone. All the employed techniques show that supratidal and intertidal carbonate facies are characterized by higher fracture frequencies than the subtidal carbonates.

To conclude, our results highlight that fracture distribution patterns with respect to the main faults are not easily predictable within a relay ramp, because they can be modulated by subsidiary faults formation and slip during the relay ramp development. Moreover, carbonate facies may play a non-negligible role in fracture distribution within fault zones hosted in shallow water carbonates. Our results therefore provide important suggestions for factors controlling fracture distribution and fluid flow within relay ramps hosted by shallow water limestones.

Acknowledgements

We thank Dr. S. Mittempergher and an anonymous reviewer for their constructive comments which helped to improve the manuscript. We thank Billy Andrews, Sabina Bigi, Carolina Giorgetti, Marco Scuderi, Luca Smeraglia, Telemaco Tesei and Fabio Trippetta for fruitful discussions, Damiano Steri for his help during the aero-photogrammetry survey, and Domenico (Mimmo) Mannetta for his help during rock samples cutting and polishing and for high-quality thin sections preparation. We acknowledge 3DFlow for providing the Education License of Zephyr Aerial. MM also thanks Manuel Curzi, Roberta Ruggieri and Lavinia Squadrilli for their help in the fieldwork and Marta Della Seta for her help with the QGIS software. This research was supported by the Sapienza University of Rome Earth Sciences Department Ph.D. funds and Sapienza Progetti di Ateneo 2017 and 2019 to EC.

References

Allmendinger, R.W., Cardozo, N., Fisher, D.M., 2012. Structural Geology Algorithms: Vectors and Tensors. Cambridge University Press.

Anders, M.H., Wiltschko, D.V., 1994. Microfracturing, paleostress and the growth of faults. Journal of Structural Geology 16, 795–815.

Aydin, A., 2000. Fractures, faults, and hydrocarbon entrapment, migration and flow. 17, 797–814. https://doi.org/10.1016/s0264-8172(00)00020-9

Bai, T., Pollard, D.D., 2000. Closely spaced fractures in layered rocks: initiation mechanism and propagation kinematics. Journal of Structural Geology 22, 1409–1425. https://doi.org/10.1016/S0191-8141(00)00062-6

Bastesen, E., & Rotevatn, A. (2012). Evolution and structural style of relay zones in layered limestone–shale sequences: insights from the Hammam Faraun Fault Block, Suez rift, Egypt. Journal of the Geological Society, 169(4), 477-488.

Bellian, J.A., Kerans, C., Jennette, D.C., 2005. Digital Outcrop Models: Applications of Terrestrial Scanning Lidar Technology in Stratigraphic Modeling. Journal of Sedimentary Research 75, 166–176. https://doi.org/10.2110/jsr.2005.013

Bemis, S.P., Micklethwaite, S., Turner, D., James, M.R., Akciz, S., Thiele, S.T., Bangash, H., 2014. Ground-based and UAV-Based photogrammetry: A multi-scale, high-resolution mapping tool for structural geology and paleoseismology. Journal of Structural Geology 69, 163–178. https://doi.org/10.1016/j.jsg.2014.10.007

Benedetti, L., Manighetti, I., Gaudemer, Y., Finkel, R., Malavieille, J., Pou, K., Arnold, M., Aumaître, G., Bourlès, D., Keddadouche, K., 2013. Earthquake synchrony and clustering on Fucino faults (Central Italy) as revealed from in situ 36Cl exposure dating. Journal of Geophysical Research: Solid Earth 118, 4948–4974. https://doi.org/10.1002/jgrb.50299

Bense, V.F., Gleeson, T., Loveless, S.E., Bour, O., Scibek, J., 2013. Fault zone hydrogeology. Earth-Science Reviews 127, 171–192. https://doi.org/10.1016/j.earscirev.2013.09.008

Berg, S.S., Skar, T., 2005. Controls on damage zone asymmetry of a normal fault zone: outcrop analyses of a segment of the Moab fault, SE Utah. Journal of Structural Geology 27, 1803–1822.

https://doi.org/10.1016/j.jsg.2005.04.012

Bigi, S., Battaglia, M., Alemanni, A., Lombardi, S., Campana, A., Borisova, E., Loizzo, M., 2013. CO2 flow through a fractured rock volume: Insights from field data, 3D fractures representation and fluid flow modeling. International Journal of Greenhouse Gas Control 18, 183–199. https://doi.org/10.1016/j.ijggc.2013.07.011

Bistacchi, A., Balsamo, F., Storti, F., Mozafari, M., Swennen, R., Solum, J., Tueckmantel, C., Taberner, C., 2015. Photogrammetric digital outcrop reconstruction, visualization with textured surfaces, and three-dimensional structural analysis and modeling: Innovative methodologies applied to fault-related dolomitization (Vajont Limestone, Southern Alps, Italy). Geosphere 11, 2031–2048. https://doi.org/10.1130/GES01005.1

Bonali, F.L., Tibaldi, A., Marchese, F., Fallati, L., Russo, E., Corselli, C., Savini, A., 2019. UAV-based surveying in volcano-tectonics: An example from the Iceland rift. Journal of Structural Geology 121, 46–64. https://doi.org/10.1016/j.jsg.2019.02.004

Brock, W.G., Engelder, T., 1977. Deformation associated with the movement of the Muddy Mountain overthrust in the Buffington window, southeastern Nevada. GSA Bulletin 88, 1667–1677. https://doi.org/10.1130/0016-7606(1977)88<1667:DAWTMO>2.0.CO;2

Caine, J.S., Evans, J.P., Forster, C.B., 1996. Fault zone architecture and permeability structure. Geology 24, 1025–1028.

Cardozo, N., Allmendinger, R.W., 2013. Spherical projections with OSXStereonet. Computers & Geosciences 51, 193–205. https://doi.org/10.1016/j.cageo.2012.07.021

Carminati, E., Lustrino, M., Cuffaro, M., Doglioni, C., 2010. Tectonics, magmatism and geodynamics of Italy: What we know and what we imagine. Journal of the Virtual Explorer 36. https://doi.org/10.3809/jvirtex.2010.00226

Casini, G., Hunt, D., Monsen, E., Bounaim, A., 2016. Fracture characterization and modeling from virtual outcrops. AAPG Bulletin 100, 41–61. https://doi.org/10.1306/09141514228

Cavinato, G.P., De Celles, P.G., 1999. Extensional basins in the tectonically bimodal central Apennines fold-thrust belt, Italy: response to corner flow above a subducting slab in retrograde motion. Geology 27, 955–958. https://doi.org/10.1130/0091-7613(1999)027<0955:EBITTB>2.3.CO;2

Cawood, A.J., Bond, C.E., Howell, J.A., Butler, R.W., Totake, Y., 2017. LiDAR, UAV or compass-clinometer? Accuracy, coverage and the effects on structural models. Journal of Structural Geology 98, 67–82. https://doi.org/10.1016/j.jsg.2017.04.004

Centamore, E., Crescenti, U., Dramis, F., 2006. Note Illustrative della Carta Geologica d'Italia alla scala 1:50.000. Foglio 368, Avezzano.

558 Chester, F.M., Evans, J.P., Biegel, R.L., 1993. Internal structure and weakening mechanisms of the
559 San Andreas fault. Journal of Geophysical Research 98, 771–786.
560 https://doi.org/10.1029/92JB01866

561

562 Chester, F., Logan, J., 1986. Implications for mechanical properties of brittle faults from
563 observations of the Punchbowl fault zone, California. Pure and Applied Geophysics 124, 79–106.
564 https://doi.org/10.1007/BF00875720

565

566 Chiaraluce, L., 2012. Unravelling the complexity of Apenninic extensional fault systems: A review
567 of the 2009 L'Aquila earthquake (Central Apennines, Italy). Journal of Structural Geology 42, 2–
568 18. https://doi.org/10.1016/j.jsg.2012.06.007

569

570 Chiaraluce, L., Stefano, D.R., Tinti, E., Scognamiglio, L., Michele, M., Casarotti, E., Cattaneo, M.,
571 Gori, D.P., Chiarabba, C., Monachesi, G., Lombardi, A., Valoroso, L., Latorre, D., Marzorati, S.,
572 2017. The 2016 Central Italy Seismic Sequence: A First Look at the Mainshocks, Aftershocks, and
573 Source Models. 88, 757–771. https://doi.org/10.1785/0220160221

574

575 Çiftci, B., Bozkurt, E., 2007. Anomalous stress field and active breaching at relay ramps: a field
576 example from Gediz Graben, SW Turkey. Geological Magazine 144, 687–699.
577 https://doi.org/10.1017/S0016756807003500

578

579 Collettini, C., Tesei, T., Scuderi, M.M., Carpenter, B.M., Viti, C., 2019. Beyond Byerlee friction,
580 weak faults and implications for slip behavior. Earth and Planetary Science Letters 519, 245–263.
581 https://doi.org/10.1016/j.epsl.2019.05.011

582

583 Colomina, I., Molina, P., 2014. Unmanned aerial systems for photogrammetry and remote sensing:
584 A review. ISPRS Journal of Photogrammetry and Remote Sensing 92, 79–97.
585 https://doi.org/10.1016/j.isprsjprs.2014.02.013

586

587 Corradetti, A., Tavani, S., Parente, M., Iannace, A., Vinci, F., Pirmez, C., Torrieri, S., Giorgioni,
588 M., Pignalosa, A., Mazzoli, S., 2017. Distribution and arrest of vertical through-going joints in a
589 seismic-scale carbonate platform exposure (Sorrento peninsula, Italy): insights from integrating
590 field survey and digital outcrop model. Journal of Structural Geology.
591 https://doi.org/10.1016/j.jsg.2017.09.009

592

593 Cosentino, D., Cipollari, P., Marsili, P., Scrocca, D., 2010. Geology of the central Apennines: a
594 regional review. 36. https://doi.org/10.3809/jvirtex.2010.00223

595

596 Cowie, P., Phillips, R., Roberts, G., McCaffrey, K., Zijerveld, L., Gregory, L., Walker, F.J.,
597 Wedmore, L., Dunai, T., Binnie, S., Freeman, S., Wilcken, K., Shanks, R., Huismans, R.,
598 Papanikolaou, I., Michetti, A., Wilkinson, M., 2017. Orogen-scale uplift in the central Italian
599 Apennines drives episodic behaviour of earthquake faults. Scientific Reports 7, 44858.
600 https://doi.org/10.1038/srep44858

601

602 D'Agostino, N., Giuliani, R., Mattone, M., Bonci, L., 2001a. Active crustal extension in the Central
603 Apennines (Italy) inferred from GPS measurements in the interval 1994–1999. Geophysical
604 Research Letters 28, 2121–2124. https://doi.org/10.1029/2000GL012462

D'Agostino, N., Jackson, J., Dramis, F., Funiciello, R., 2001b. Interactions between mantle upwelling, drainage evolution and active normal faulting: an example from the central Apennines (Italy). Geophysical Journal International 147, 475–497. https://doi.org/10.1046/j.1365-246X.2001.00539.x

D'Argenio, B., Ferreri, V., Amodio, S., & Pelosi, N. (1997). Hierarchy of high-frequency orbital cycles in Cretaceous carbonate platform strata. Sedimentary Geology, 113(3-4), 169-193.

De Paola, N., Collettini, C., Faulkner, D. R., & Trippetta, F. (2008). Fault zone architecture and deformation processes within evaporitic rocks in the upper crust. *Tectonics*, *27*(4).

Destro, N., 1995. Release fault: A variety of cross fault in linked extensional fault systems, in the Sergipe-Alagoas Basin, NE Brazil. Journal of Structural Geology 17, 615–629.

Devoti, R., Pietrantonio, G., Pisani, A., Riguzzi, F., Serpelloni, E., 2010. Present day kinematics of Italy. 36. https://doi.org/10.3809/jvirtex.2010.00237

Doglioni, C., 1991. A proposal for the kinematic modelling of W dipping subductions possible applications to the Tyrrhenian Apennines system. Terra Nova 3, 423–434.

Dor, O., Ben-Zion, Y., Rockwell, T., Brune, J., 2006a. Pulverized rocks in the Mojave section of the San Andreas Fault Zone. Earth and Planetary Science Letters 245, 642–654. https://doi.org/10.1016/j.epsl.2006.03.034

Dor, O., Rockwell, T., Ben-Zion, Y., 2006b. Geological Observations of Damage Asymmetry in the Structure of the San Jacinto, San Andreas and Punchbowl Faults in Southern California: A Possible Indicator for Preferred Rupture Propagation Direction. Pure and Applied Geophysics 163, 301–349. https://doi.org/10.1007/s00024-005-0023-9

Faulkner, D., Mitchell, T., Healy, D., Heap, M., 2006. Slip on "weak" faults by the rotation of regional stress in the fracture damage zone. Nature 444, nature05353. https://doi.org/10.1038/nature05353

Fossen, H., Johansen, T. E. S., Hesthammer, J., & Rotevatn, A. (2005). Fault interaction in porous sandstone and implications for reservoir management; examples from southern Utah. *AAPG bulletin*, *89*(12), 1593-1606.

Fossen, H., Rotevatn, A., 2016. Fault linkage and relay structures in extensional settings—A review. Earth-Science Reviews 154, 14–28. https://doi.org/10.1016/j.earscirev.2015.11.014

Galadini, F., Galli, P., 1999. The Holocene paleoearthquakes on the 1915 Avezzano earthquake faults (central Italy): implications for active tectonics in the central Apennines. Tectonophysics 308, 143–170. https://doi.org/10.1016/S0040-1951(99)00091-8

Giorgetti, C., Collettini, C., Scuderi, M., Barchi, M.R., Tesei, T., 2016. Fault geometry and mechanics of marly carbonate multilayers: An integrated field and laboratory study from the Northern Apennines, Italy. 93. https://doi.org/10.1016/j.jsg.2016.10.001

Giuffrida, A., Agosta, F., Rustichelli, A., Panza, E., La Bruna, V., Eriksson, M., ... & Giorgioni, M. (2019). Fracture stratigraphy and DFN modelling of tight carbonates, the case study of the Lower Cretaceous carbonates exposed at the Monte Alpi (Basilicata, Italy). Marine and Petroleum Geology, 104045.

Gratier, J.-P., Renard, F., Labaume, P., 1999. How pressure solution creep and fracturing processes interact in the upper crust to make it behave in both a brittle and viscous manner. Journal of Structural Geology 21, 1–9. https://doi.org/10.1016/s0191-8141(99)00035-8

Gudmundsson, A., Berg, S.S., Lyslo, K.B., Skurtveit, E., 2001. Fracture networks and fluid transport in active fault zones. Journal of Structural Geology 23, 343–353. https://doi.org/10.1016/S0191-8141(00)00100-0

Gudmundsson, A., Simmenes, T.H., Larsen, B., Philipp, S.L., 2010. Effects of internal structure and local stresses on fracture propagation, deflection, and arrest in fault zones. Journal of Structural Geology 32, 1643–1655. https://doi.org/10.1016/j.jsg.2009.08.013

Healy, D., Rizzo, R.E., Cornwell, D.G., Farrell, N., Watkins, H., Timms, N.E., Gomez-Rivas, E., Smith, M., 2017. FracPaQ: A MATLAB™ toolbox for the quantification of fracture patterns. Journal of Structural Geology 95, 1–16. https://doi.org/10.1016/j.jsg.2016.12.003

Huang, Q., Angelier, J., 1989. Fracture spacing and its relation to bed thickness. 126, 355–362.

https://doi.org/10.1017/S0016756800006555

Kattenhorn, S., Aydin, A., Pollard, D., 2000. Joints at high angles to normal fault strike: an explanation using 3-D numerical models of fault-perturbed stress fields. Journal of Structural Geology 22, 1–23. https://doi.org/10.1016/S0191-8141(99)00130-3

Kim, Y.-S., Peacock, D., Sanderson, D., 2004. Fault damage zones. Journal of Structural Geology 26, 503–517. https://doi.org/10.1016/j.jsg.2003.08.002

Ladeira, F.L., Price, N.J., 1981. Relationship between fracture spacing and bed thickness. Journal of Structural Geology 3, 179-183.

Larsen, B, Grunnaleite, I., Gudmundsson, A., 2010a. How fracture systems affect permeability development in shallow-water carbonate rocks: An example from the Gargano Peninsula, Italy. Journal of Structural Geology 32, 1212–1230. https://doi.org/10.1016/j.jsg.2009.05.009

Larsen, B, Gudmundsson, A., Grunnaleite, I., Sælen, G., Talbot, M.R., Buckley, S.J., 2010b. Effects of sedimentary interfaces on fracture pattern, linkage, and cluster formation in peritidal carbonate rocks. Marine and Petroleum Geology 27, 1531–1550. https://doi.org/10.1016/j.marpetgeo.2010.03.011

Marrett, R., Allmendinger, R.W., 1990. Kinematic analysis of fault slip data. Journal of Structural Geology. 973-986.

McCaffrey, K., Holdsworth, R., Imber, J., Clegg, P., Paola, N., Jones, R., Hobbs, R., Holliman, N., Trinks, I., 2005a. Putting the geology back into Earth models. Eos, Transactions American Geophysical Union 86, 461–466. https://doi.org/10.1029/2005EO460001

McCaffrey, K.J.W., Jones, R.R., Holdsworth, R.E., Wilson, R.W., Clegg, P., Imber, J., Holliman, N., Trinks, I., 2005b. Unlocking the spatial dimension: digital technologies and the future of geoscience fieldwork. Journal of the Geological Society 162, 927–938. https://doi.org/10.1144/0016-764905-017

McGinnis, R.N., Ferrill, D.A., Morris, A.P., Smart, K.J., Lehrmann, D., 2017. Mechanical stratigraphic controls on natural fracture spacing and penetration. Journal of Structural Geology 95, 160–170.

Mercuri, M., McCaffrey, K. J., Smeraglia, L., Mazzanti, P., Collettini, C., & Carminati, E. (2020). Complex geometry and kinematics of subsidiary faults within a carbonate-hosted relay ramp. *Journal of Structural Geology*, *130*, 103915.

Michie, E., Haines, T., Healy, D., Neilson, J., Timms, N., Wibberley, C., 2014. Influence of carbonate facies on fault zone architecture. Journal of Structural Geology 65, 82–99. https://doi.org/10.1016/j.jsg.2014.04.007

Miller, S.A., Collettini, C., Chiaraluce, L., Cocco, M., Barchi, M.R., Kaus, B.J., 2004. Aftershocks

722 driven by a high-pressure CO2 source at depth. 427, 724–727. https://doi.org/10.1038/nature02251

723

724 Mitchell, T.M., Ben-Zion, Shimamoto, 2011. Pulverized fault rocks and damage asymmetry along
725 the Arima-Takatsuki Tectonic Line, Japan. Earth and Planetary Science Letters 308, 284–297.
726 https://doi.org/10.1016/j.epsl.2011.04.023

727

728 Mitchell, T.M., Faulkner, D.R., 2009. The nature and origin of off-fault damage surrounding strike-
729 slip fault zones with a wide range of displacements: A field study from the Atacama fault system,
730 northern Chile. Journal of Structural Geology 31, 802–816.
731 https://doi.org/10.1016/j.jsg.2009.05.002

732

733 Morewood, N.C., Roberts, G.P., 2000. The geometry, kinematics and rates of deformation within an
734 en échelon normal fault segment boundary, central Italy. Journal of Structural Geology 22, 1027–
735 1047. https://doi.org/10.1016/S0191-8141(00)00030-4

736

737 Narr, W., Suppe, J., 1991. Joint spacing in sedimentary rocks. Journal of Structural Geology 13,
738 1037–1048. https://doi.org/10.1016/0191-8141(91)90055-N

739

740 Nur, A., Booker, J.R., 1972. Aftershocks Caused by Pore Fluid Flow? Science 175, 885–887.
741 https://doi.org/10.1126/science.175.4024.885

742

743 Odling, N.E., Gillespie, P., Bourgine, B., Castaing, C., Chiles, J.P., Christensen, N.P., Fillion, E.,
744 Genter, A., Olsen, C., Thrane, L. and Trice, R., 1999. Variations in fracture system geometry and
745 their implications for fluid flow in fractures hydrocarbon reservoirs. *Petroleum Geoscience, 5,* 373-

384.

Olariu, M.I., Ferguson, J.F., Aiken, C., Xu, X., 2008. Outcrop fracture characterization using terrestrial laser scanners: Deep-water Jackfork sandstone at Big Rock Quarry, Arkansas. Geosphere 4, 247–259. https://doi.org/10.1130/GES00139.1

Osleger, D. (1991). Subtidal carbonate cycles: Implications for allocyclic vs. autocyclic controls. Geology, 19(9), 917-920.

Peacock, D.C.P., Dimmen, V., Rotevatn, A., Sanderson, D.J., 2017. A broader classification of damage zones. Journal of Structural Geology 102, 179–192. https://doi.org/10.1016/j.jsg.2017.08.004

Peacock, D.C.P., Parfitt, E.A., 2002. Active relay ramps and normal fault propagation on Kilauea Volcano, Hawaii. Journal of Structural Geology 24, 729–742. https://doi.org/10.1016/S0191-8141(01)00109-2

Peacock, D.C.P., Price, S.P., Whitham, A.G., Pickles, C.S., 2000. The World's biggest relay ramp: Hold With Hope, NE Greenland. Journal of Structural Geology 22, 843–850. https://doi.org/10.1016/S0191-8141(00)00012-2

Peacock, D.C.P., Xing, Z., 1994. Field examples and numerical modelling of oversteps and bends along normal faults in cross-section. Tectonophysics 234, 147–167. https://doi.org/10.1016/0040-1951(94)90209-7

771 Pless, J., McCaffrey, K., Jones, R., Holdsworth, R., Conway, A., Krabbendam, M., 2015. 3D
772 characterization of fracture systems using Terrestrial Laser Scanning: an example from the
773 Lewisian basement of NW Scotland. Geological Society, London, Special Publications 421, 125–
774 141. https://doi.org/10.1144/SP421.14
775
776 Pollard, D.D., Aydin, A.A., 1988. Progress in understanding jointing over the past century.
777 Geological Society of America Bulletin 100, 1181–1204.
778
779 Priest, S.D., Hudson, J.A., 1981. Estimation of discontinuity spacing and trace length using scanline
780 surveys. Int. J. Rock Mech. Min. Sci. & Geomech. Abstr 18, 183–197.
781
782 Renard, F., Dysthe, D., Feder, J., Bjørlykke, K. and Jamtveit, B, 2001. Enhanced pressure solution
783 creep rates induced by clay particles: Experimental evidence in salt aggregates.
784 https://doi.org/10.1029/2000GL012394
785
786 Rotevatn, A., Fossen, H., Hesthammer, J., Aas, T., Howell, J., 2007. Are relay ramps conduits for
787 fluid flow? Structural analysis of a relay ramp in Arches National Park, Utah. Geological Society,
788 London, Special Publications 270, 55–71. https://doi.org/10.1144/GSL.SP.2007.270.01.04
789
790 Rustichelli, A., Torrieri, S., Tondi, E., Laurita, S., Strauss, C., Agosta, F., Balsamo, F., 2016.
791 Fracture characteristics in Cretaceous platform and overlying ramp carbonates: An outcrop study
792 from Maiella Mountain (central Italy). Marine and Petroleum Geology 76, 68–87.
793 https://doi.org/10.1016/j.marpetgeo.2016.05.020
794

795 Rutter, E.H., 1983. Pressure solution in nature, theory and experiment. Journal of the Geological
796 Society 140, 725–740. https://doi.org/10.1144/gsjgs.140.5.0725
797
798 Sanderson, D., Nixon, C. (2015). The use of topology in fracture network characterization Journal
799 of Structural Geology 72, 55-66. https://dx.doi.org/10.1016/j.jsg.2015.01.005
800
801 Savage, H., Brodsky, E., 2011. Collateral damage: Evolution with displacement of fracture
802 distribution and secondary fault strands in fault damage zones. Journal of Geophysical Research:
803 Solid Earth (1978–2012) 116. https://doi.org/10.1029/2010JB007665
804
805 Scognamiglio, L., Tinti, E., Casarotti, E., Pucci, S., Villani, F., Cocco, M., Magnoni, F., Michelini,
806 A., Dreger, D., 2018. Complex Fault Geometry and Rupture Dynamics of the MW 6.5, 30 October
807 2016, Central Italy Earthquake. Journal of Geophysical Research: Solid Earth 123, 2943–2964.
808 https://doi.org/10.1002/2018JB015603
809
810 Seers, T.D., Hodgetts, D., 2016. Extraction of three-dimensional fracture trace maps from calibrated
811 image sequences. Geosphere 12, 1323–1340. https://doi.org/10.1130/GES01276.1
812
813 Shipton, Z.K., Cowie, P.A., 2003. A conceptual model for the origin of fault damage zone
814 structures in high-porosity sandstone. 25, 333–344.
815
816 Shipton, Z.K., Cowie, P.A., 2001. Damage zone and slip-surface evolution over μm to km scales in
817 high-porosity Navajo sandstone, Utah. Journal of Structural Geology 23, 1825–1844.
818

819 Sibson, R.H., 1994. Crustal stress, faulting and fluid flow. Geological Society, London, Special
820 Publications 78, 69–84. https://doi.org/10.1144/GSL.SP.1994.078.01.07
821
822 Sibson, R.H., 1996. Structural permeability of fluid-driven fault-fracture meshes. Journal of
823 Structural Geology 18, 1031–1042. https://doi.org/10.1016/0191-8141(96)00032-6
824
825 Smeraglia, L., Berra, F., Billi, A., Boschi, C., Carminati, E., Doglioni, C., 2016. Origin and role of
826 fluids involved in the seismic cycle of extensional faults in carbonate rocks. Earth and Planetary
827 Science Letters 450, 292–305. https://doi.org/10.1016/j.epsl.2016.06.042
828
829 Smeraglia, L., Billi, A., Carminati, E., Cavallo, A., Toro, G., Spagnuolo, E., Zorzi, F., 2017. Ultra-
830 thin clay layers facilitate seismic slip in carbonate faults. 7, 974. https://doi.org/10.1038/s41598-
831 017-00717-4
832
833 Smith, S.A., Billi, A., Toro, G., Spiess, R., 2011. Principal Slip Zones in Limestone:
834 Microstructural Characterization and Implications for the Seismic Cycle (Tre Monti Fault, Central
835 Apennines, Italy). Pure and Applied Geophysics 168, 2365–2393. https://doi.org/10.1007/s00024-
836 011-0267-5
837
838 Strasser, A., Pittet, B., Hillgartner, H. and Pasquier, J.-B. (1999) Depositional sequences in shallow
839 carbonate dominated sedimentary systems: concepts for a highresolution analysis. Sed. Geol., 128,
840 201–221.
841
842 Tavani, S., Granado, P., Corradetti, A., Girundo, M., Iannace, A., Arbués, P., Muñoz, J.A., Mazzoli,

S., 2014. Building a virtual outcrop, extracting geological information from it, and sharing the results in Google Earth via OpenPlot and Photoscan: An example from the Khaviz Anticline (Iran). Computers & Geosciences 63, 44–53. https://doi.org/10.1016/j.cageo.2013.10.013

Tavani, S., Storti, F., Salvini, F., Toscano, C., 2008. Stratigraphic versus structural control on the deformation pattern associated with the evolution of the Mt. Catria anticline, Italy. Journal of Structural Geology 30, 664–681. https://doi.org/10.1016/j.jsg.2008.01.011

Telling, J., Lyda, A., Hartzell, P., Reviews, G.C., 2017. Review of earth science research using terrestrial laser scanning.

Terzaghi, R.D., 1965. Sources of error in joint surveys. Géotechnique 15 (3), 287–304. http://dx.doi.org/10.1680/geot.1965.15.3.287

Townend, J., Zoback, M.D., 2000. How faulting keeps the crust strong. 28, 399–402. https://doi.org/10.1130/0091-7613(2000)028

Vasuki, Y., Holden, E.-J., Kovesi, P., Micklethwaite, S., 2014. Semi-automatic mapping of geological Structures using UAV-based photogrammetric data: An image analysis approach. Computers & Geosciences 69, 22–32. https://doi.org/10.1016/j.cageo.2014.04.012

Vinci, F., Tavani, S., Iannace, A., Parente, M., Pirmez, C., Torrieri, S., Giorgioni, M., Pignalosa, A., Mazzoli, S., 2018. Extracting and quantifying fracture patterns from a reservoir-scale Virtual

866 Outcrop Model. *EGU General Assembly Conference Abstracts* (Vol. 20, p. 4797).

867

868 Volatili, T., Zambrano, M., Cilona, A., Huisman, H., Rustichelli, A., Giorgioni, M., Vittori, S.,
869 Tondi, E., 2019. From fracture analysis to flow simulations in fractured carbonates: The case study
870 of the Roman Valley Quarry (Majella Mountain, Italy). Marine and Petroleum Geology 100, 95–
871 110. https://doi.org/10.1016/j.marpetgeo.2018.10.040

872

873 Wennberg, O., Svånå, T., Azizzadeh, M., Aqrawi, A., Brockbank, P., Lyslo, K., Ogilvie, S., 2006.
874 Fracture intensity vs. mechanical stratigraphy in platform top carbonates: the Aquitanian of the
875 Asmari Formation, Khaviz Anticline, Zagros, SW Iran. Petroleum Geoscience 12, 235–246.
876 https://doi.org/10.1144/1354-079305-675

877

878 Westoby, M.J., Brasington, J., Glasser, N.F., Hambrey, M.J., Reynolds, J.M., 2012. 'Structure-
879 from-Motion' photogrammetry: A low-cost, effective tool for geoscience applications.
880 Geomorphology 179, 300–314. https://doi.org/10.1016/j.geomorph.2012.08.021

881

882 Wilkinson, M.W., Jones, R.R., Woods, C.E., Gilment, S.R., McCaffrey, K.J.W., Kokkalas, S.,
883 Long, J.J., 2016. A comparison of terrestrial laser scanning and structure-from-motion
884 photogrammetry as methods for digital outcrop acquisition. Geosphere 12, 1865–1880.
885 https://doi.org/10.1130/GES01342.1

886

887 Wilson, J., Chester, J., Chester, F., 2003. Microfracture analysis of fault growth and wear processes,
888 Punchbowl Fault, San Andreas system, California. Journal of Structural Geology 25, 1855–1873.

https://doi.org/10.1016/S0191-8141(03)00036-1

Woodcock, N.H., Mort, K., 2008. Classification of fault breccias and related fault rocks. Geological Magazine 145, 435–440. https://doi.org/10.1017/s0016756808004883

Wu, H., Pollard, D.D., 1995. An experimental study of the relationship between joint spacing and layer thickness. Journal of Structural Geology 17, 887–905. https://doi.org/10.1016/0191-8141(94)00099-L

Figure captions

Figure 1 – Geological setting of the analysed outcrop. (A) Simplified geological map of the Fucino basin in the central Apennines, Italy (the black arrow in the upper right inset indicates the location). SPCF: San Potito – Celano Fault. (B) Simplified geological map of the Tre Monti fault area and zoom of the studied area. (C) Panoramic view of the study outcrop. Stereoplots with Linked Bingham solution in (B) and (C) show the overall kinematics of the Tre Monti fault and of the front fault segment in the relay ramp respectively. P: pressure axis; T: tension axis. Blue and red dots are P and T axis calculated individually for each slickenside data. Kinematic inversions have been performed using FaultKin (Marrett and Allmendinger, 1990; Allmendinger et al., 2012).

Figure 2 -Lithological characterization of the damage zone host rock. (A) Cartoon representing the hypothesized depositional environment of the limestones in the quarry: the transition between a tidal flat and a lagoon carbonate platform environment. The subtidal facies content increases moving toward the lagoon environment. (B) Representation of an ideal peritidal cycle with the associated carbonate facies. (C) Example of an outcrop where supratidal and intertidal facies, characterized by centimetric to decimetric thick beds, predominate. (D) Outcrop characterized by

914 the predominance of subtidal facies and characterized by > 1 m thick beds. (E-J): scans (E-G) and
915 optical micrographs at plane polarized light (H-I) of samples pertaining to the supratidal (E, H),
916 intertidal (F, I), and subtidal (G, J) carbonate facies.
917
918 Figure 3 – Scanlines. Example of a scanline survey (SL13, see Section S1 for the location) and
919 linear fracture frequency calculation. L: scanline length; N: number of fractures intercepted by the
920 scanline; P10: linear fracture frequency.
921
922 Figure 4 – Fracture analysis on the oriented samples. (A) Collected rock sample with marked
923 orientation. (B) Fracture traces digitized on a high-resolution scan of the sample (dark blue lines).
924 (C) The linear fracture frequency has been calculated by counting the fracture traces sampled by
925 sub-horizontal scanlines (yellow lines). (D) Other fracturing parameters such as areal fracture
926 frequency and fracture intensity have been calculated by using the FracPaQ software (Healy et al.,
927 2017).
928
929 Figure 5 – Fracture analysis on the virtual outcrop. (A) Unmanned Aerial Vehicle survey in the
930 study outcrop. (B) Virtual outcrop model of the quarry obtained by a structure-from-motion
931 processing. (C) Example of an orthorectified panels with 1 mm per pixel resolution extracted from
932 the virtual outcrop model. A1-12 indicate the label of the virtual scan-areas (D) Example of a
933 virtual scan-area (A3). (E, F) The orthorectified squares were interpreted by drawing fractures
934 (yellow lines in panel E), bedding (green lines in panel E), and supratidal/intertidal carbonate facies
935 (F). The fracture analysis was performed using FracPaQ software (Healy et al., 2017).
936
937 Figure 6 – Fracture frequency and geometry. (A) Space distribution of the linear (diamonds, P10)
938 and areal (circles, P20) fracture frequencies respectively measured along scanlines and obtained
939 from virtual scan-areas. The minor faults traces are retrieved from Mercuri et al. (2020). The

940 stereoplots (Schmidt's net, low hemisphere) show the density contour of the poles to fractures in
941 different sectors of the quarry (see inset in the upper left). The label of the scanlines used as input
942 are reported in brackets (B) Density contour plot of the poles to the fractures collected along the
943 scanlines.
944
945 Figure 7 – Foliated breccias. Photo (A) and interpretation (B) of an exposure of foliated breccias. B:
946 bedding, F: foliation, J: joints, SS: slip surfaces. The location of the photo is reported in Figure 6.
947
948 Figure 8 – Evolution of the linear and areal fracture frequency with distance from the front segment
949 of the relay ramp respectively measured through scanlines (blue) and virtual scan-areas (red).
950
951 Figure 9 – Relationship between fracture frequency and carbonate facies. (A) Box plot showing
952 fracture frequency for different carbonate facies in scanlines (B) Box plot showing fracture
953 frequency for different carbonate facies in oriented samples (C) Fracture frequency vs. supratidal
954 and intertidal facies content in virtual scan-areas.
955
956 Figure 10 – Structural control on the fracture frequency. The fracture frequency increases with
957 density of subsidiary faults that increases moving from SE to NW in the quarry, i.e., approaching
958 the centre of the relay ramp.
959
960 Figure 11 – Facies distribution in the quarry. (A) Map of the quarry showing the percentage of
961 supratidal and intertidal carbonate facies measured in the virtual-scan areas. The supratidal and
962 intertidal content is higher in the north-western sector of the quarry. High supratidal/intertidal facies
963 contents are often accompanied by the development of foliated breccias. (B) Supratidal and
964 intertidal carbonate facies content with distance from front segment (i.e. moving toward NW).
965

966 Figure 12 – Damage evolution versus supratidal and intertidal facies content. (A) The alternation of
967 supratidal/intertidal and subtidal carbonate facies promotes a mechanical stratigraphy. The higher
968 fracture intensity observed in the supratidal and intertidal facies can be related to smaller thickness
969 of the beds (cm- to dm-thick, whilst the subtidal facies is characterized by m-thick beds) and to the
970 development of compartmentalized fractures. The supratidal portions can contain small amount of
971 clay minerals. (B) The average fracture intensity increases with increasing supratidal/intertidal
972 content for a fixed sampling area (C) Foliated breccias can eventually develop in portions of the
973 quarry dominated by the supratidal facies.
974
975 Figure 13 – Hypotheses for the role of carbonate facies on fracture intensity distribution. (A)
976 Carbonate facies define a mechanical stratigraphy at metre scale, with highly damaged supratidal
977 intervals but has no effect on fracture intensity distribution at hundreds of meters scale. (B)
978 Supratidal facies distribution guides the intensity of subsidiary faults and fractures at hundreds of
979 meters scale. Pleistocene continental breccias (see Fig. 1b) cropping out in the relay zone are not
980 represented in the cartoon.
981

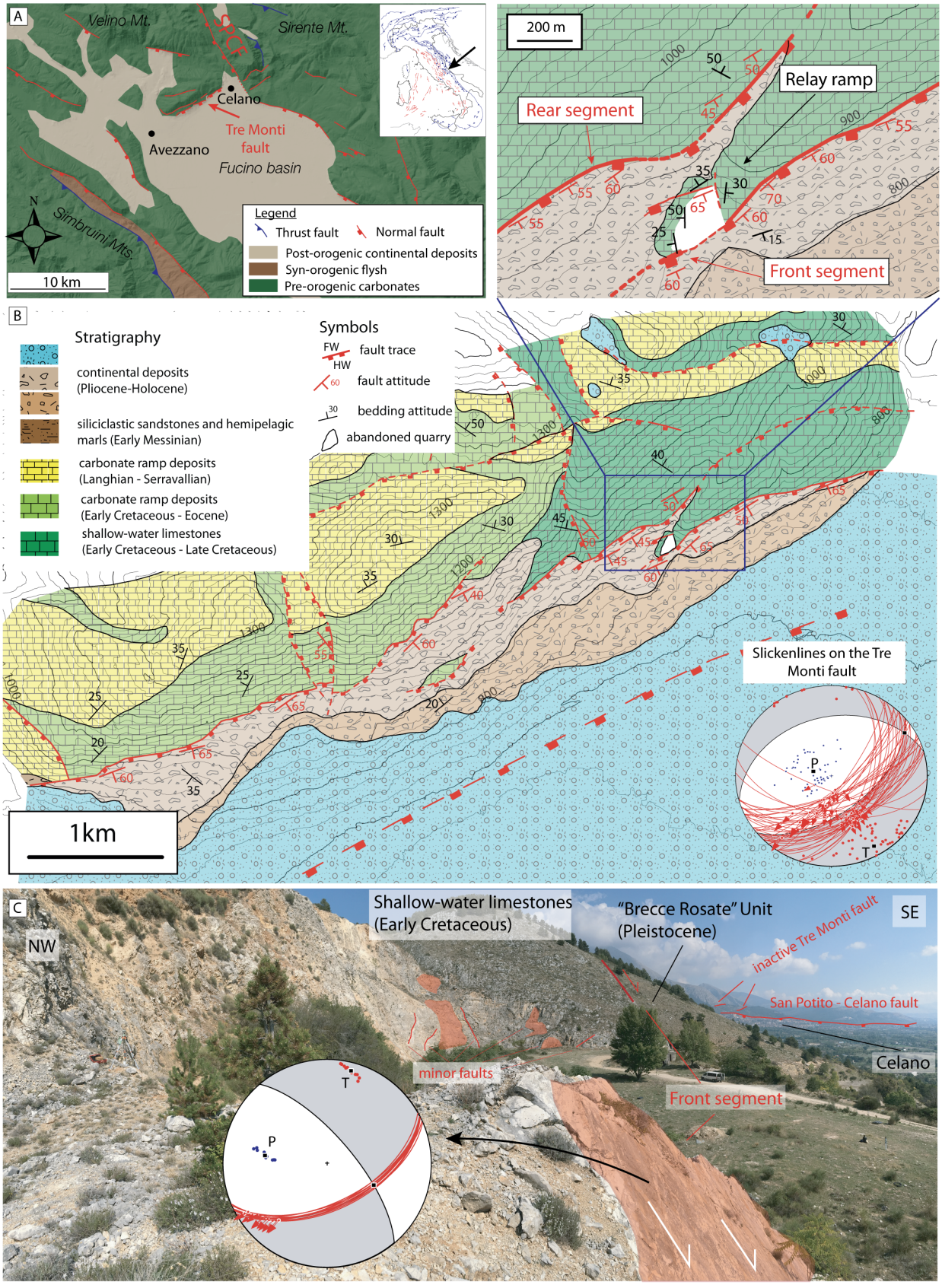
A
Velino Mt.
Sirente Mt.
SACF
Celano
Avezzano
Tre Monti fault
Fucino basin
Simbruini Mts.
N
10 km
Legend
Thrust fault
Normal fault
Post-orogenic continental deposits
Syn-orogenic flysh
Pre-orogenic carbonates
200 m
Relay ramp
Rear segment
Front segment
B
Stratigraphy
continental deposits (Pliocene-Holocene)
siliciclastic sandstones and hemipelagic marls (Early Messinian)
carbonate ramp deposits (Langhian - Serravallian)
carbonate ramp deposits (Early Cretaceous - Eocene)
shallow-water limestones (Early Cretaceous - Late Cretaceous)
Symbols
FW
HW
fault trace
fault attitude
bedding attitude
abandoned quarry
Slickenlines on the Tre Monti fault
P
T
1km
C
NW
SE
Shallow-water limestones (Early Cretaceous)
"Brecce Rosate" Unit (Pleistocene)
inactive Tre Monti fault
San Potito - Celano fault
Celano
minor faults
Front segment
T
P

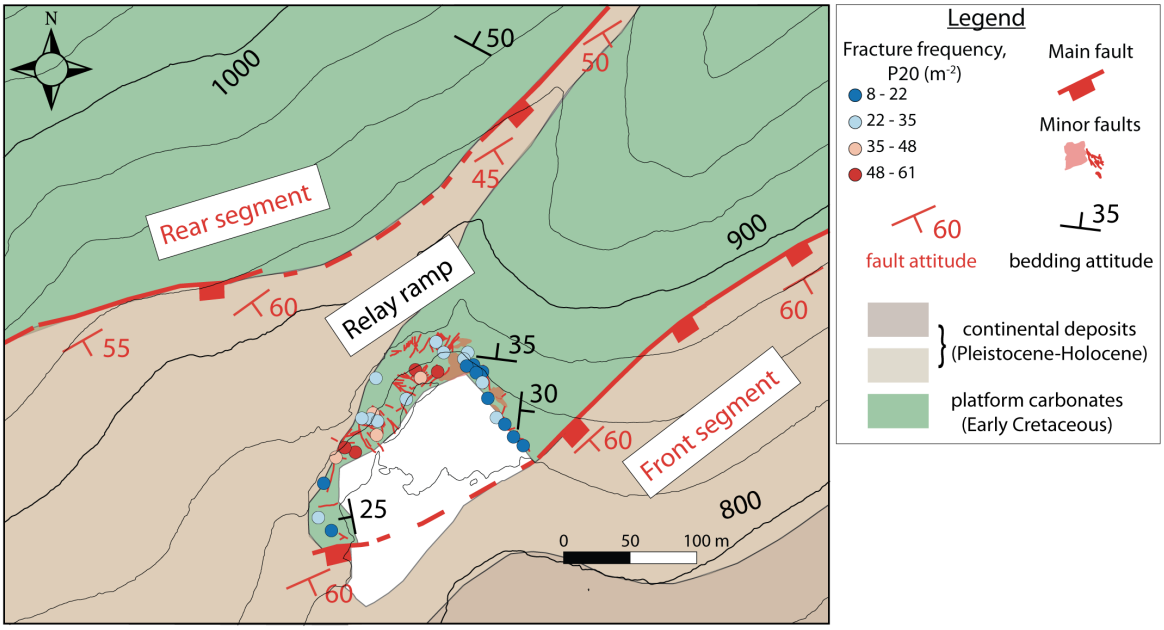
N
1000
50
50
45
Rear segment
900
Relay ramp
60
55
35
30
60
60
Front segment
25
800
60
0
50
100 m
Legend
Fracture frequency, P20 (m-2)
8 - 22
22 - 35
35 - 48
48 - 61
Main fault
Minor faults
60
fault attitude
35
bedding attitude
continental deposits (Pleistocene-Holocene)
platform carbonates (Early Cretaceous)

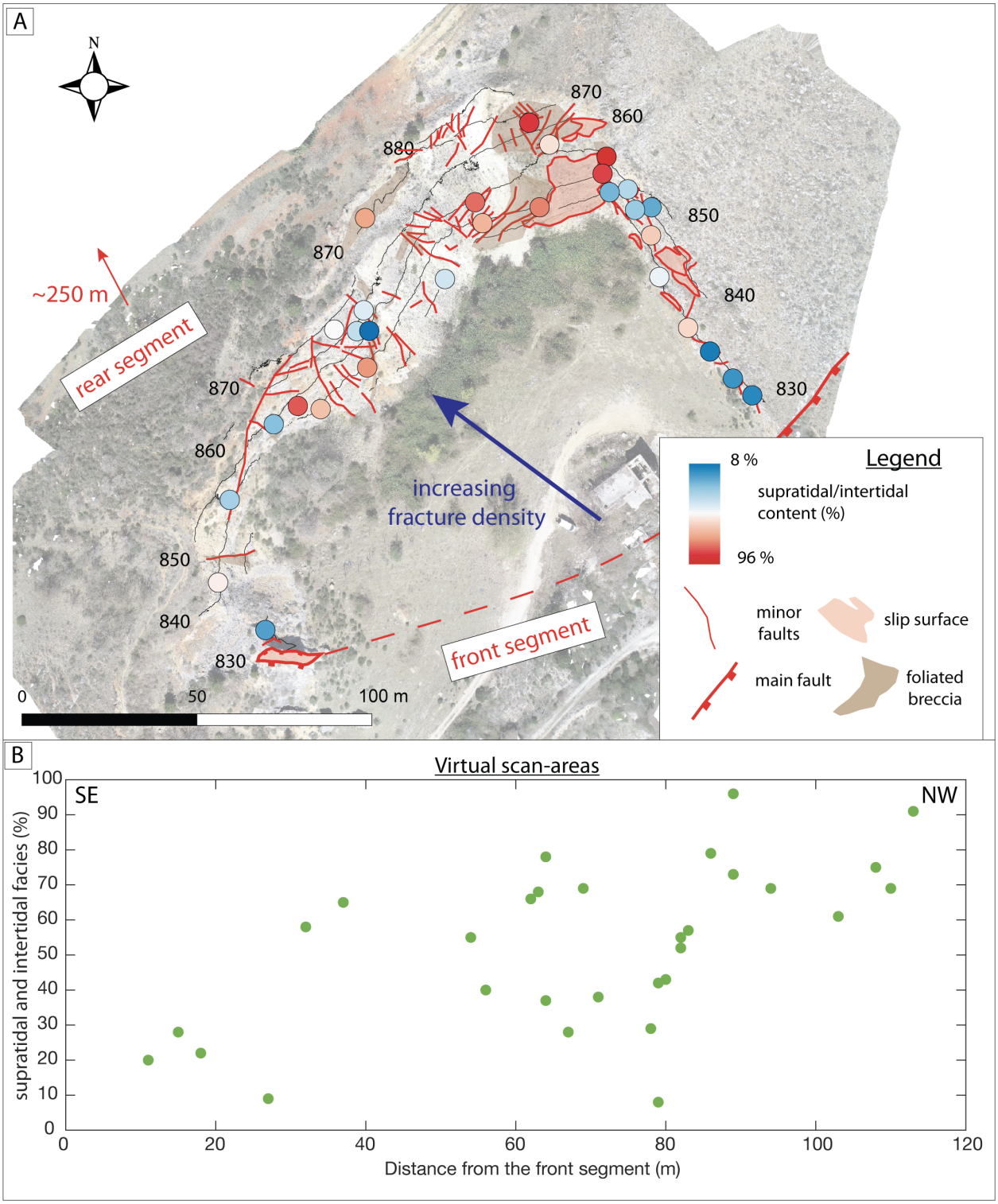
A
N
870
860
880
850
870
840
~250 m
rear segment
870
830
860
increasing
fracture density
850
840
front segment
830
0
50
100 m
Legend
8 %
supratidal/intertidal
content (%)
96 %
minor
faults
slip surface
main fault
foliated
breccia
B
Virtual scan-areas
SE
NW
supratidal and intertidal facies (%)
Distance from the front segment (m)
0
10
20
30
40
50
60
70
80
90
100
0
20
40
60
80
100
120

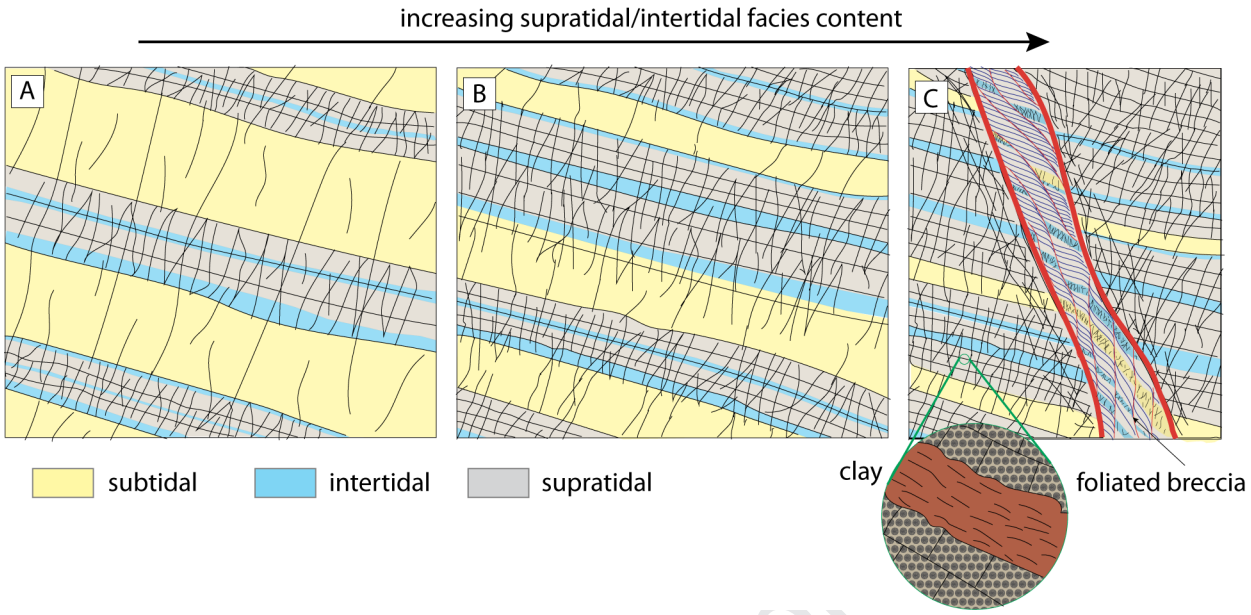

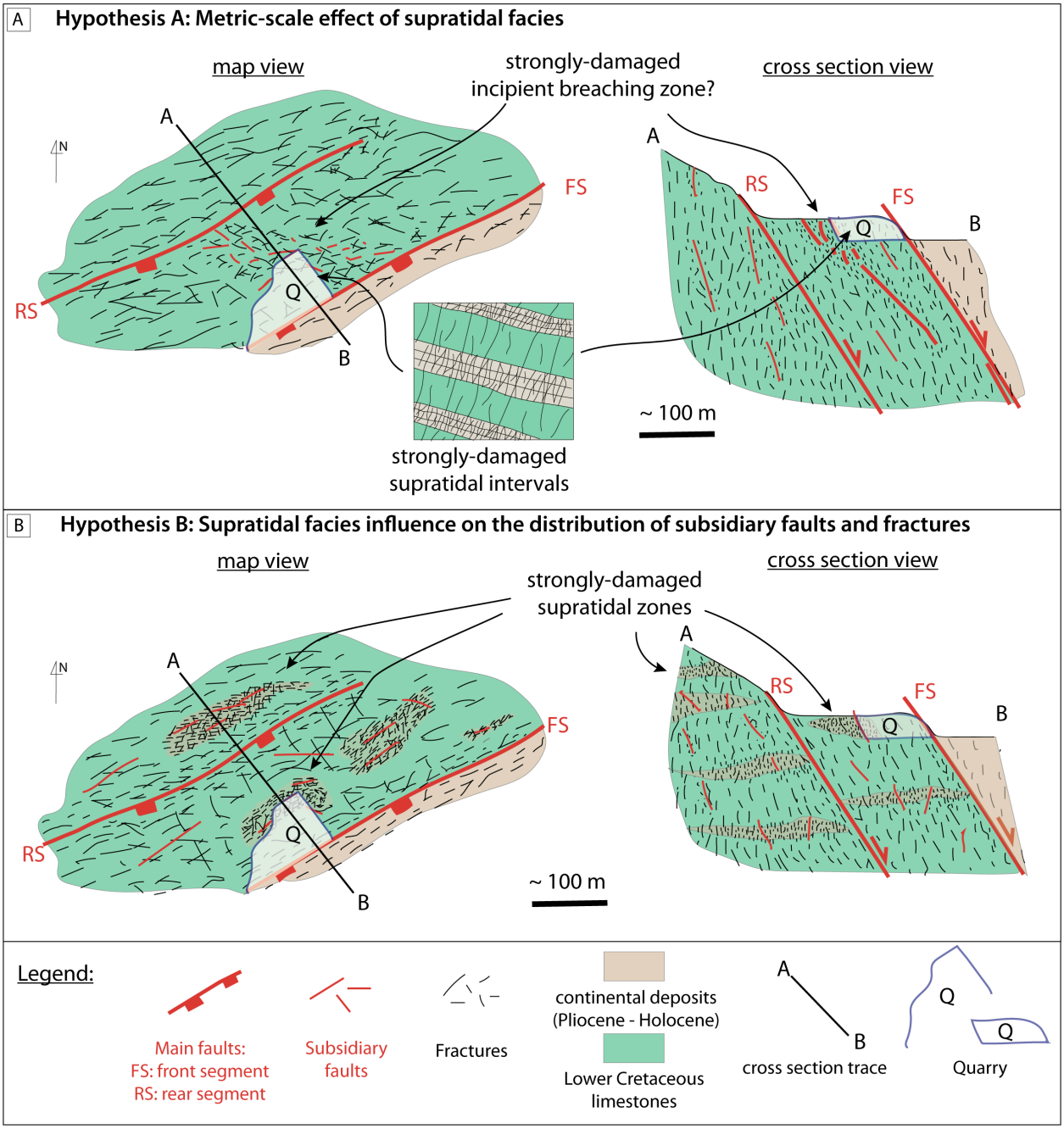
A
Hypothesis A: Metric-scale effect of supratidal facies
map view
strongly-damaged
incipient breaching zone?
cross section view
A
N
FS
RS
Q
B
A
RS
FS
Q
B
~ 100 m
strongly-damaged
supratidal intervals
B
Hypothesis B: Supratidal facies influence on the distribution of subsidiary faults and fractures
map view
strongly-damaged
supratidal zones
cross section view
A
N
FS
RS
Q
B
A
RS
FS
Q
B
~ 100 m
Legend:
Main faults:
FS: front segment
RS: rear segment
Subsidiary
faults
Fractures
continental deposits
(Pliocene - Holocene)
Lower Cretaceous
limestones
A
B
cross section trace
Q
Q
Quarry

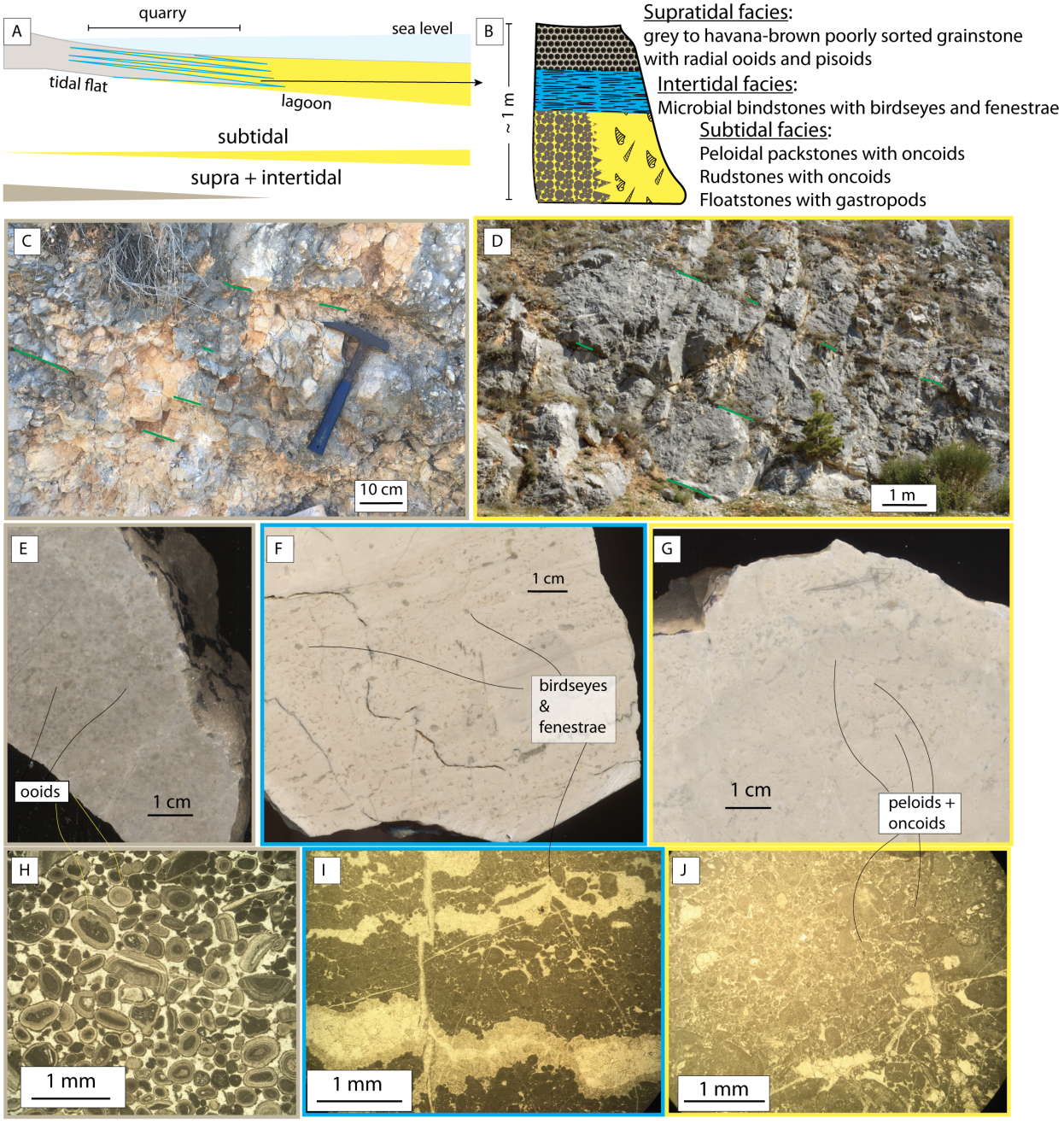
A
quarry
sea level
tidal flat
lagoon
subtidal
supra + intertidal
B
~ 1 m
Supratidal facies:
grey to havana-brown poorly sorted grainstone
with radial ooids and pisoids
Intertidal facies:
Microbial bindstones with birdseyes and fenestrae
Subtidal facies:
Peloidal packstones with oncoids
Rudstones with oncoids
Floatstones with gastropods
C
10 cm
D
1 m
E
ooids
1 cm
F
1 cm
birdseyes
&
fenestrae
G
1 cm
peloids +
oncoids
H
1 mm
I
1 mm
J
1 mm

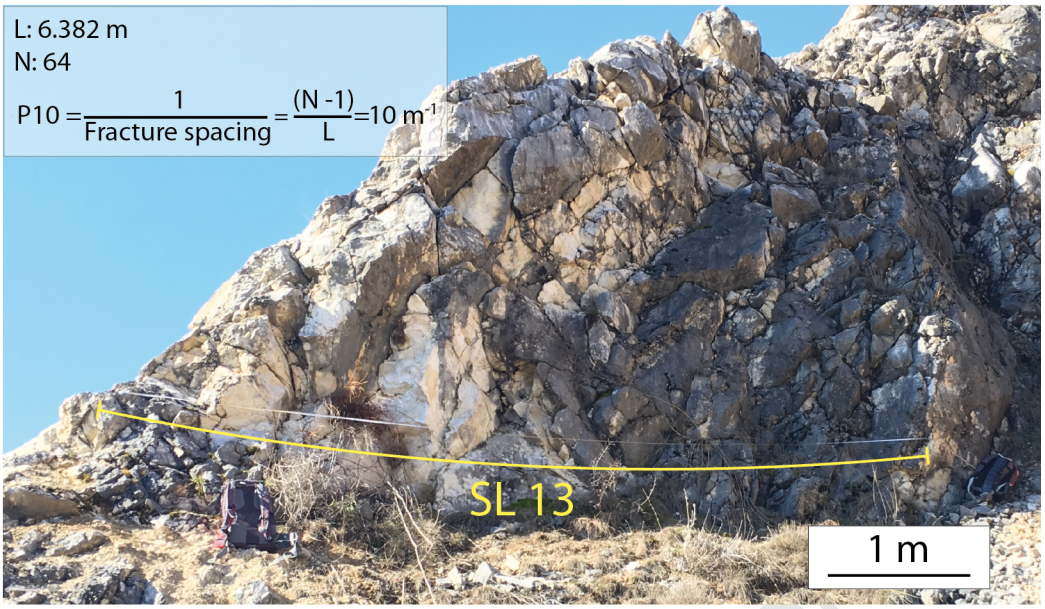

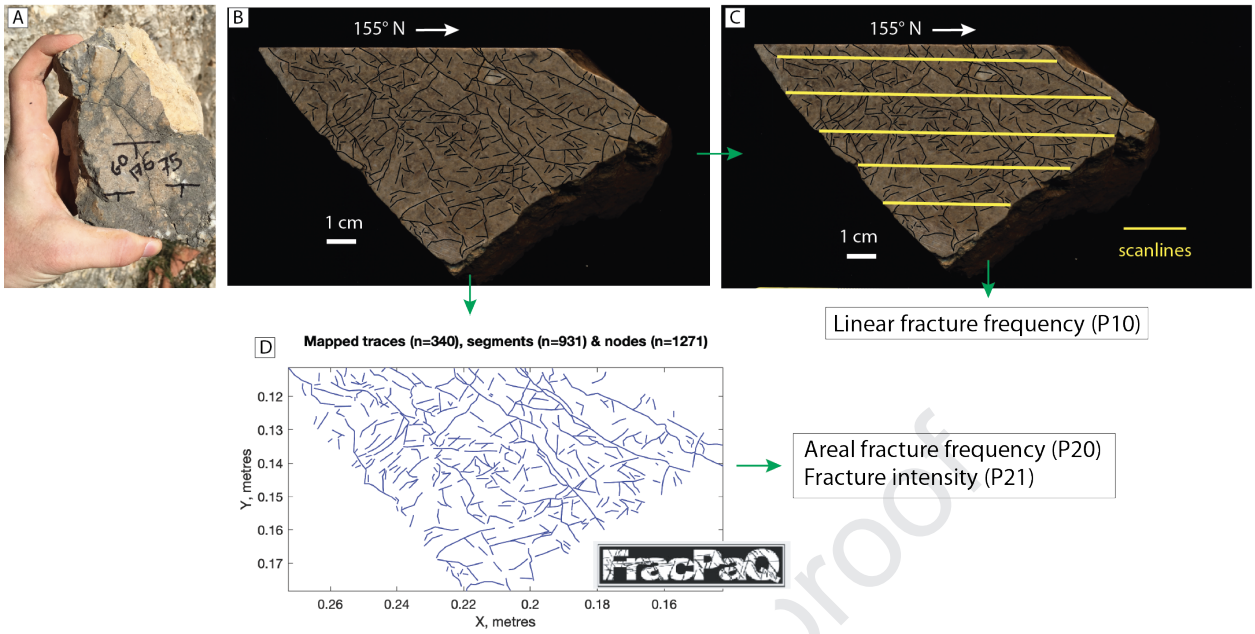

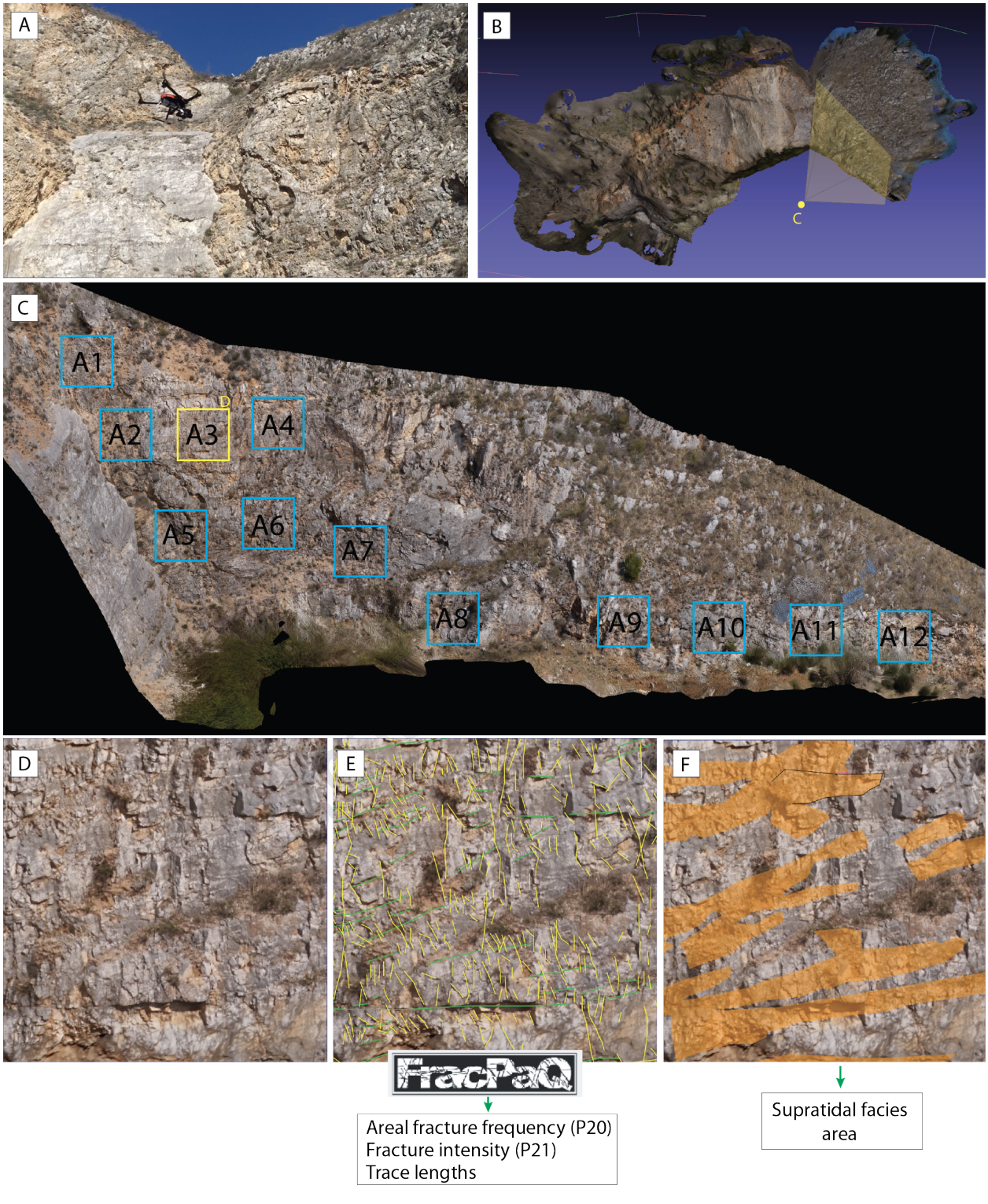
A
B
C
C
A1
A2
A3
D
A4
A5
A6
A7
A8
A9
A10
A11
A12
D
E
F
FracPaQ
Areal fracture frequency (P20)
Fracture intensity (P21)
Trace lengths
Supratidal facies area

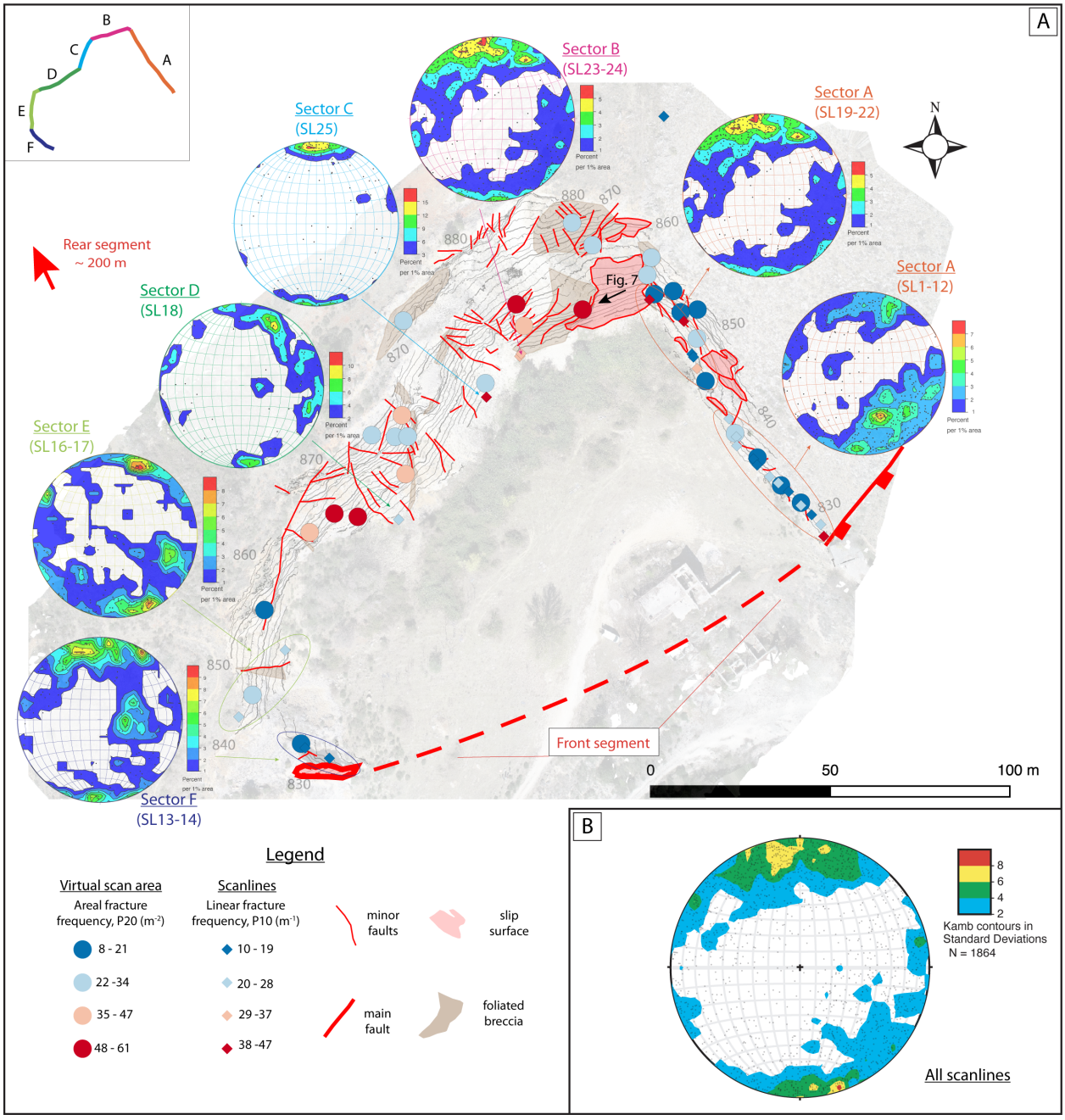
A
B
C
D
E
F
Sector B
(SL23-24)
Sector C
(SL25)
Sector A
(SL19-22)
N
Rear segment
~ 200 m
Sector D
(SL18)
Fig. 7
Sector A
(SL1-12)
Sector E
(SL16-17)
Front segment
0
50
100 m
Sector F
(SL13-14)
Legend
Virtual scan area
Areal fracture frequency, P20 (m-2)
8 - 21
22 -34
35 - 47
48 - 61
Scanlines
Linear fracture frequency, P10 (m-1)
10 - 19
20 - 28
29 -37
38 -47
minor faults
slip surface
main fault
foliated breccia
B
Kamb contours in Standard Deviations
N = 1864
All scanlines

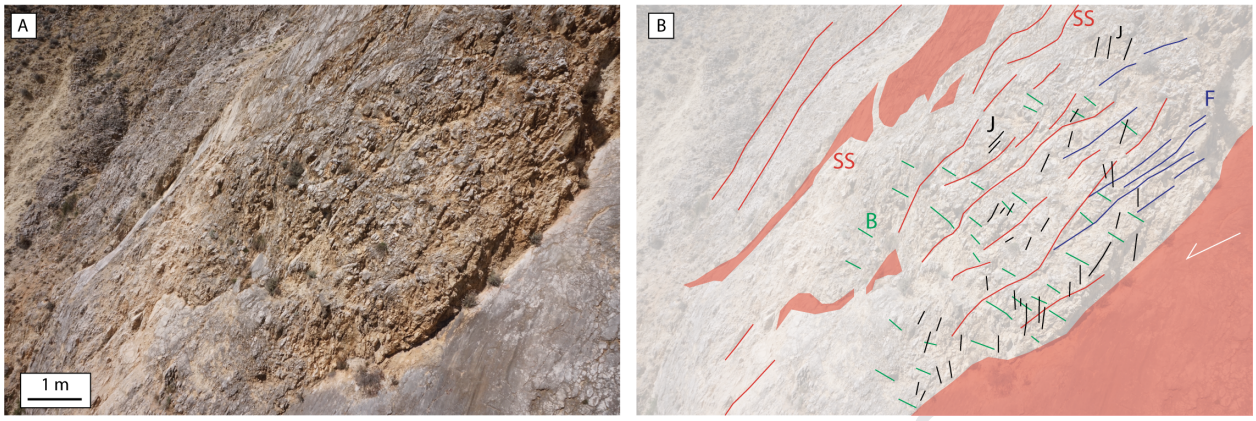

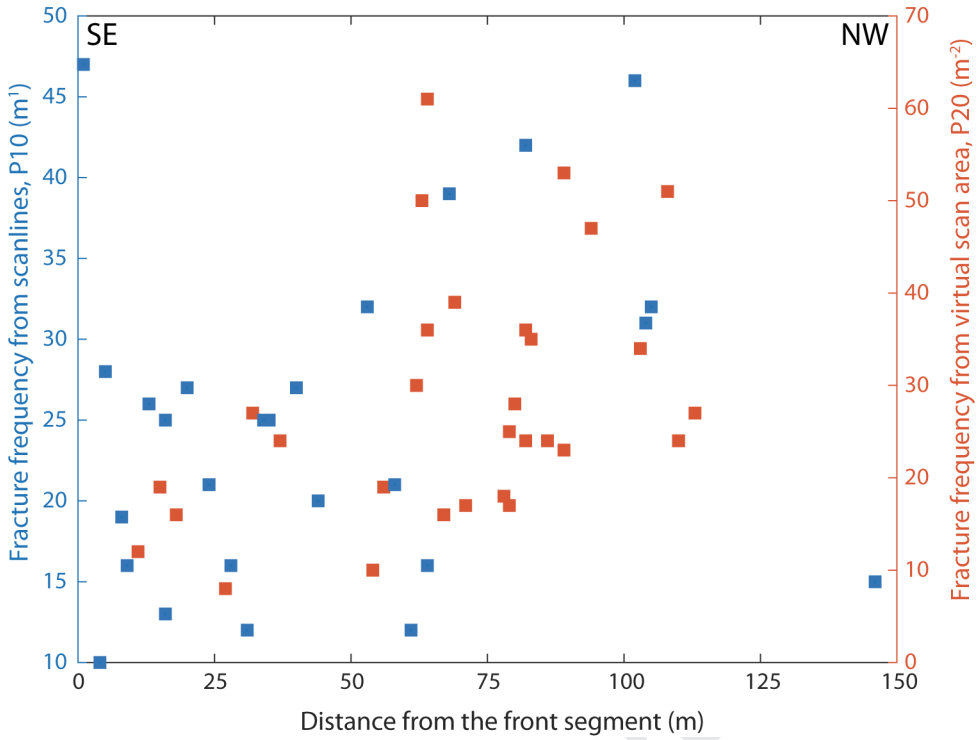

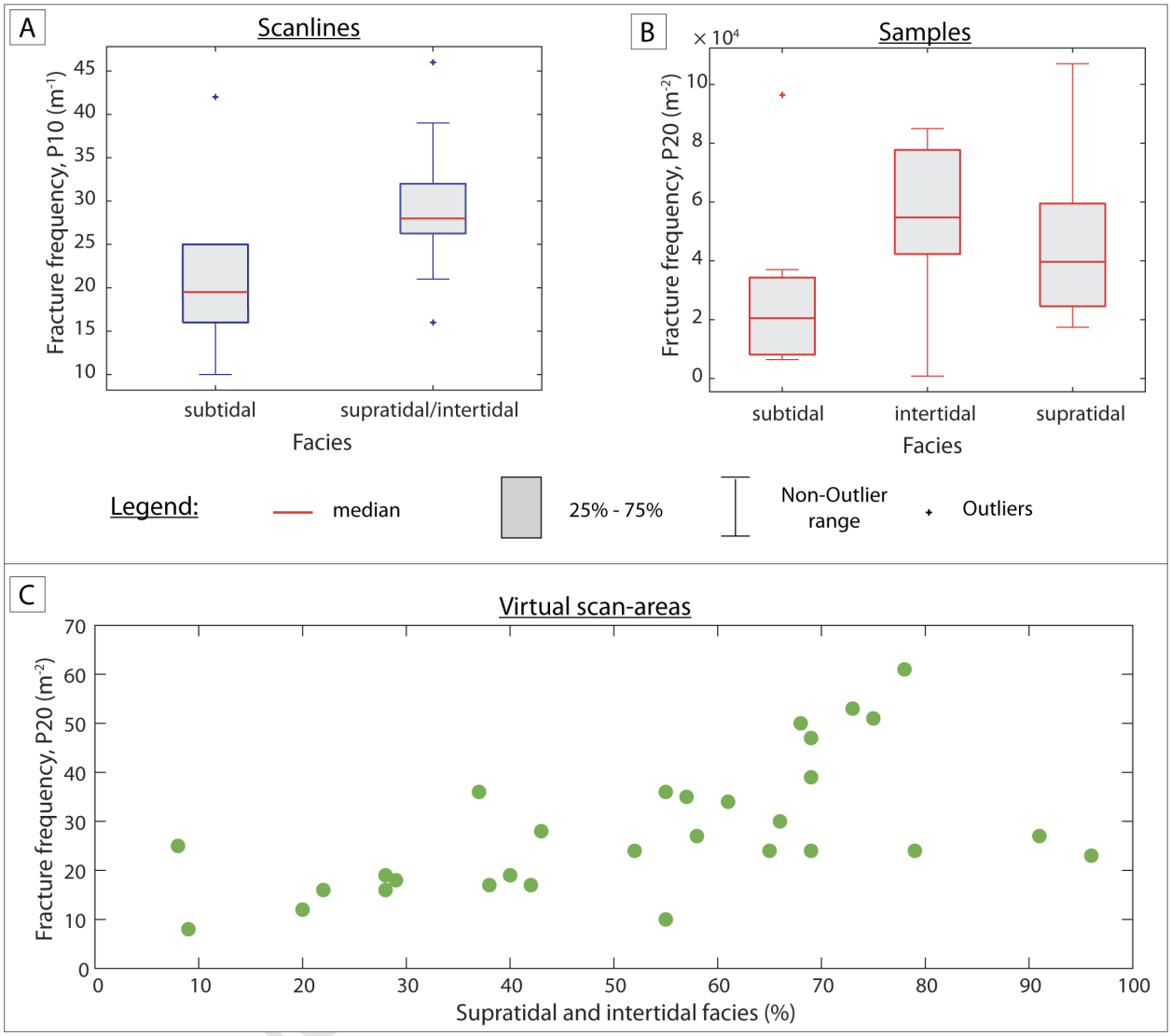
A
Scanlines
Fracture frequency, P10 (m-1)
45
40
35
30
25
20
15
10
subtidal
supratidal/intertidal
Facies
B
× 10^4
Samples
Fracture frequency, P20 (m-2)
10
8
6
4
2
0
subtidal
intertidal
supratidal
Facies
Legend:
median
25% - 75%
Non-Outlier range
Outliers
C
Virtual scan-areas
Fracture frequency, P20 (m-2)
70
60
50
40
30
20
10
0
0
10
20
30
40
50
60
70
80
90
100
Supratidal and intertidal facies (%)

Highlights

- Analysis of fracture distribution within a carbonate-hosted relay ramp
- Integration of scanlines, oriented rock samples and a virtual outcrop model
- Fracture frequency increases with distance from the front segment of the relay ramp
- Subsidiary faults and carbonate peritidal facies control fracture distribution

Declaration of interests

☒ The authors declare that they have no known competing financial interests or personal relationships that could have appeared to influence the work reported in this paper.

☐The authors declare the following financial interests/personal relationships which may be considered as potential competing interests: